

Railway rolling noise in curved tracks: Dynamic modelling of the wheelset and influence of the curve

V. T. Andrés^a, J. Martínez-Casas^{a,*}, F. D. Denia^a, D. J. Thompson^b, S. Bruni^c

^a*Instituto de Ingeniería Mecánica y Biomecánica, Universitat Politècnica de València, Camino de Vera s/n, 46022 Valencia, Spain*

^b*Institute of Sound and Vibration Research, University of Southampton, Southampton SO17 1BJ, United Kingdom*

^c*Department of Mechanical Engineering, Politecnico di Milano, via La Masa 1, Milan 20156, Italy*

Abstract

Railway wheelsets operating on curved tracks experience complex dynamic behaviour which can affect the generation of rolling noise. This paper presents a comprehensive study on the dynamic response of wheelsets on curved tracks and the associated rolling noise radiation from the wheel and track. A dynamic model is developed to accurately compute the vibrational response of the flexible wheelset, considering the inertial effects associated with its rotation and trajectory along the curved track. An axisymmetric approach is proposed, which reduces significantly the computational effort in comparison to a three-dimensional numerical model. Considering a railway vehicle and its interaction with the track, the rolling noise generated in curved conditions is evaluated. Noise radiated as a result of a vehicle running on curves of 300 m and 2 km radius is compared with a tangent track. Differences in the sound radiation are found among the acoustic levels associated with each wheelset, the steady-state position of such wheelsets on the rails being a key factor.

Keywords:

Curved railway track, Rotating wheelset, Dynamic model, Axisymmetry, Railway rolling noise, Curve influence

1. Introduction

Railways are a significant contributor to sustainable mobility, offering an environmentally friendly and efficient mode of transportation for both passengers and freight. However, noise emission from railway lines remains a major environmental issue that has been increasingly recognized as a significant challenge. Among the sources of sound radiation from railway vehicles, curve squeal and rolling noise are two of the most important [1]. The former is characterized by a high-pitched tonal sound, often arising in sharp curves due to a number of complex phenomena, such as self-excited vibration of a wheel caused by unsteady lateral

*Corresponding author

Email addresses: vicanrui@upv.es (V. T. Andrés), jomarc12@mcm.upv.es (J. Martínez-Casas), fdenia@mcm.upv.es (F. D. Denia), djt@isvr.soton.ac.uk (D. J. Thompson), stefano.bruni@polimi.it (S. Bruni)

forces [2, 3]. The latter, on the other hand, is generated by the interaction between the wheels and track in the presence of roughness on the wheel and rail rolling surfaces inducing vertical excitation [4]. Due to its nature, squeal noise is strongly linked to running on curved track (according to [4], it is less likely to occur in curves of radius greater than 200 m). Most studies of rolling noise, however, have focused on tangent track, although it is present on curved tracks as well. Furthermore, curved segments often exhibit rail corrugation, which can lead to higher rolling noise levels [5, 6]. Hence, the investigation of rolling noise for curved tracks takes on significance. Wang *et al.* [7] used a time-domain model for the vehicle/track interaction to simulate the vehicle curving behaviour and to study rolling noise on curved tracks. Their analysis involved assessing noise emissions from the inner side of the wheelset/track interaction on curves with varying radii. Their findings revealed that as track curvature increased, higher sound pressure levels were observed, primarily because of increased lateral rail vibration as a consequence of higher lateral forces. While the previous work provides valuable insights into rolling noise on curved tracks, additional research and mathematical modelling is needed to understand this phenomenon and to support the identification of mitigation measures.

When a railway vehicle negotiates a curve, the lateral displacement and angle of attack of the wheelset cause a change in the position, size, and shape of the wheel/rail contact patch as well as slip velocities within the contact area [8–11]. This affects the wheel/rail interaction forces and thus influences the levels of noise radiation compared with running on a tangent track. To accurately assess rolling noise emission in curve conditions, an advanced model of the railway vehicle is needed. In such conditions, the vehicle behaviour can be characterized as a superposition of the steady-state regime and the dynamic oscillations [12]. The former is commonly described with a multibody model which accounts for the centrifugal effects induced by the curved trajectory, while a high frequency model of the wheelsets is necessary for the latter. To this end, Martínez-Casas *et al.* [13] initially proposed an Eulerian approach to model the wheelset on a tangent track, which was subsequently extended to consider its motion along a curved track through the incorporation of a trajectory coordinate set [14]. Later, Andrés *et al.* [15] adopted an axisymmetric approach for the aforementioned wheelset model in a tangent track, thereby reducing the computational calculation time by three orders of magnitude. However, this efficient model does not account for the inertial effects of the curved trajectory and, to the authors’ knowledge, no axisymmetric wheelset model considering these inertial effects has been presented so far.

In this work, the wheelset model for a curved trajectory presented in reference [14] is formulated first in a cylindrical reference system and, subsequently, an axisymmetric approach is proposed by expanding the displacements of the flexible body around the circumferential direction, yielding a much more efficient model. Using the above wheelset model, rolling noise radiated by a single wheelset and a complete vehicle while running through a curve is evaluated. To do this, the steady-state conditions during curving are simulated using the VI-Rail software [16] and then the dynamic behaviour around these conditions is studied. The wheelset dynamics are described through the aforementioned model, while the track is characterized using wave propagation theory [17, 18]. A frequency-domain model of the vehicle/track interaction is then proposed, which allows the wheel/rail contact forces to be solved. Later, the wheelset sound radiation is determined by applying an acoustic model based on the use of radiation ratios [19], whereas the track radiation is computed using a methodology

based on equivalent acoustic sources [20]. Finally, the noise radiated in two different curving conditions is compared with the acoustic levels in a tangent track, analysing the effect of the curving condition on the rolling noise. While, as previously mentioned, corrugation might alter rail roughness on different curves, the present study is concerned with the effect of curved tracks for the same assumed roughness.

Following this introduction, Section 2 presents a three-dimensional model of the railway wheelset which incorporates the inertial effects associated with running on curved tracks. In Section 3, an axisymmetric approach is introduced as an alternative method to investigate the wheelset behaviour on curved tracks, offering faster computational performance without sacrificing accuracy. Section 4 focuses on the dynamic model of the vehicle, track, and wheel/rail interaction. Section 5 presents the results of the numerical simulations and analyses, revealing valuable insights into the influence of the curve on noise generation. Finally, Section 6 summarizes the conclusions and suggests potential avenues for future research.

2. Three-dimensional dynamic model of the wheelset

In this section, the three-dimensional dynamic model developed in [14] is formulated in a cylindrical frame. To do this, three different reference systems are defined: an inertial (fixed) Cartesian system $\mathbf{u}_{0,1}\mathbf{u}_{0,2}\mathbf{u}_{0,3}$, a trajectory coordinate Cartesian frame $\mathbf{u}_{c,1}\mathbf{u}_{c,2}\mathbf{u}_{c,3}$ travelling with the wheelset and a cylindrical frame also travelling with the wheelset with coordinates (r,θ,z) , as defined in Fig. 1; the last two frames are centred in the undeformed configuration of the wheelset (midpoint of the axle) and will be referred to as track frames. To denote a variable in different reference systems, the subscript 0 indicates the inertial one, the subscript c represents the travelling Cartesian frame, and no subscript is used for the travelling cylindrical frame. Thus, for an arbitrary variable Φ , the following relationships hold:

$$\begin{aligned}\Phi_0 &= \mathbf{T}\Phi_c, \\ \Phi_c &= \mathbf{\Theta}\Phi,\end{aligned}\tag{1}$$

where the matrices \mathbf{T} and $\mathbf{\Theta}$ are defined as follows:

$$\mathbf{T} = \begin{bmatrix} \cos(\beta) & -\sin(\beta)\cos(\gamma) & \sin(\beta)\sin(\gamma) \\ \sin(\beta) & \cos(\beta)\cos(\gamma) & -\cos(\beta)\sin(\gamma) \\ 0 & \sin(\gamma) & \cos(\gamma) \end{bmatrix},\tag{2}$$

$$\mathbf{\Theta} = \begin{bmatrix} -\sin(\theta) & -\cos(\theta) & 0 \\ 0 & 0 & 1 \\ -\cos(\theta) & \sin(\theta) & 0 \end{bmatrix},\tag{3}$$

with β being the track angle, defined as a rotation around the $\mathbf{u}_{0,3}$ vector, and γ being the cant angle, defined as a rotation around the $\mathbf{u}_{c,1}$ vector, as can be seen in Fig. 1. Note that, in the case of a right-hand curve, β is negative while γ is positive. It is also worth indicating that, according to the definition of $\mathbf{\Theta}$, the radial coordinate is contained in the 1_c - 3_c plane.

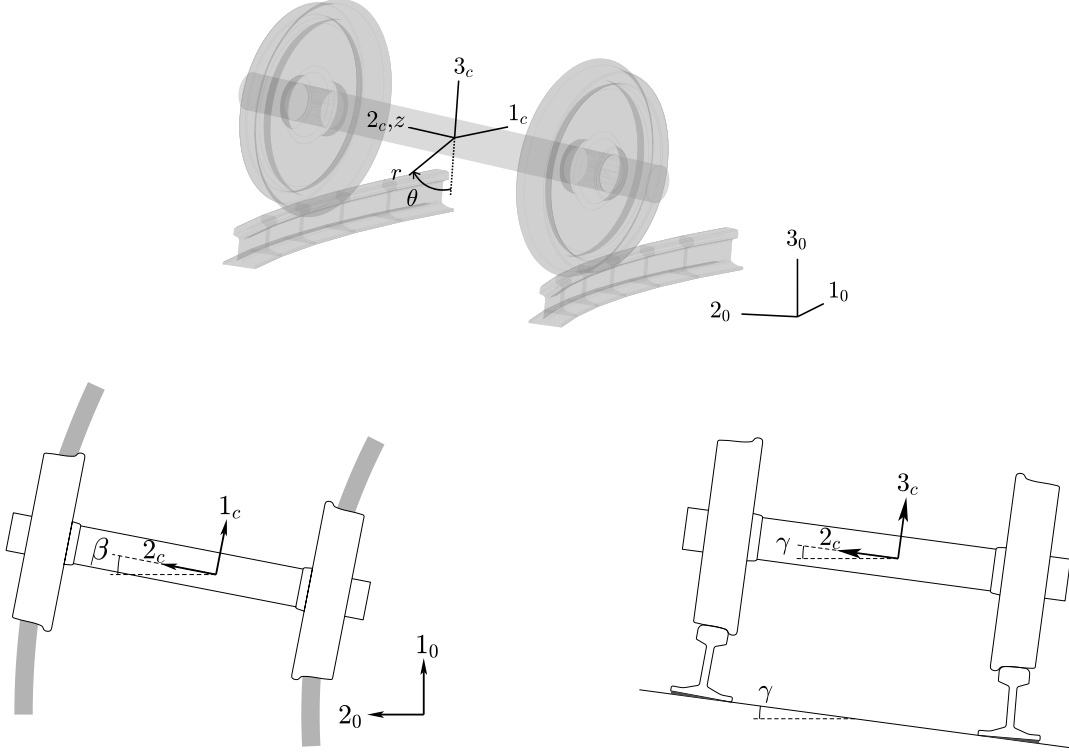


Fig. 1: Definition of the reference systems.

Considering the motion of the flexible wheelset, the position \mathbf{q}_0 of any particle of this in the deformed shape formulated in the inertial reference system can be expressed as follows:

$$\mathbf{q}_0 = \mathbf{p}_0 + \mathbf{T}\Theta(\mathbf{u} + \mathbf{w}(\mathbf{u}, t)), \quad (4)$$

where \mathbf{p}_0 defines the position of the travelling frames, $\mathbf{u} = (r \ 0 \ z)^T$ is the spatial position corresponding to that particle in the undeformed configuration and $\mathbf{w} = (w_r \ w_\theta \ w_z)^T$ contains the displacements of the particle at the position \mathbf{u} and instant t due to the body flexibility and small rigid body motion (RBM) in the radial, circumferential, and axial directions, respectively. The velocity of that particle of the wheelset expressed in the inertial reference system can be written as [21, 22]:

$$\frac{D\mathbf{q}_0}{Dt} = \dot{\mathbf{p}}_0 + \dot{\mathbf{T}}\Theta(\mathbf{u} + \mathbf{w}) + \mathbf{T}\Theta \frac{D(\mathbf{u} + \mathbf{w})}{Dt}, \quad (5)$$

where $\frac{D(\mathbf{u} + \mathbf{w})}{Dt}$ represents the velocity of the wheelset particle expressed in the cylindrical frame when running on a tangent track which is given by Eq. (17) of [15]. For convenience, the velocity of the particle is now formulated in the Cartesian frame using the relation in Eq. (1), yielding:

$$\frac{D\mathbf{q}_c}{Dt} = \dot{\mathbf{p}}_c + \tilde{\omega}_c \Theta(\mathbf{u} + \mathbf{w}) + \Theta \frac{D(\mathbf{u} + \mathbf{w})}{Dt}, \quad (6)$$

where $\tilde{\omega}_c = \mathbf{T}^T \dot{\mathbf{T}}$ is the angular velocity matrix of the track frames expressed in the Cartesian travelling frame. The kinetic energy K of the railway wheelset is thus given by:

$$\begin{aligned}
K &= \frac{1}{2} \int_V \rho \frac{D\mathbf{q}_c^T}{Dt} \frac{D\mathbf{q}_c}{Dt} dV \\
&= \frac{1}{2} \dot{\mathbf{p}}_c^T \dot{\mathbf{p}}_c M + \dot{\mathbf{p}}_c^T \tilde{\omega}_c \int_V \rho \Theta (\mathbf{u} + \mathbf{w}) dV + \dot{\mathbf{p}}_c^T \int_V \rho \Theta \frac{D(\mathbf{u} + \mathbf{w})}{Dt} dV \\
&\quad + \frac{1}{2} \int_V \rho (\mathbf{u} + \mathbf{w})^T \Theta^T \tilde{\omega}_c^T \tilde{\omega}_c \Theta (\mathbf{u} + \mathbf{w}) dV + \int_V \rho (\mathbf{u} + \mathbf{w})^T \Theta^T \tilde{\omega}_c^T \Theta \frac{D(\mathbf{u} + \mathbf{w})}{Dt} dV + K_t,
\end{aligned} \tag{7}$$

where ρ and V are, respectively, the density and volume of the wheelset, $dV = rd\theta dr dz$, and K_t is the kinetic energy of the wheelset when running on a tangent track (further details are given in Eq. (18) of reference [15]).

In this work, a model based on the Finite Element Method (FEM) is utilized, wherein the computation of the displacement field in the e th element of the FE mesh is accomplished through interpolation of the nodal solution using the following approach:

$$\mathbf{w}(r, \theta, z, t) = \mathbf{N}(r, \theta, z) \mathbf{w}^e(t), \tag{8}$$

where the shape function matrix \mathbf{N} and the vector \mathbf{w}^e with the displacements or degrees of freedom (DoF) can be expressed as indicated in Eqs. (22) and (23) of [15], respectively. The terms of the Lagrange equations associated with the wheelset kinetic energy in Eq. (7), when this is applied to the e th element of the FE mesh, can be evaluated as follows:

$$\begin{aligned}
\frac{D}{Dt} \left(\frac{\partial K}{\partial \dot{\mathbf{w}}^e} \right)^T - \left(\frac{\partial K}{\partial \mathbf{w}^e} \right)^T &= 2\mathbf{P}^e \dot{\mathbf{w}}^e + (2\Omega \mathbf{S}^e + \mathbf{R}^e + \mathbf{B}^e) \mathbf{w}^e - 2\Omega \mathbf{U}^e - \mathbf{H}^e - \mathbf{L}^e \\
&\quad - \mathbf{G}^e \mathbf{T}^T \ddot{\mathbf{p}}_0 + \left(\frac{D}{Dt} \left(\frac{\partial K_t}{\partial \dot{\mathbf{w}}^e} \right)^T - \left(\frac{\partial K_t}{\partial \mathbf{w}^e} \right)^T \right).
\end{aligned} \tag{9}$$

where a constant rotational speed Ω of the wheelset about its main axis is assumed. The last term in Eq. (9) considers the contribution to the Lagrange equations of the kinetic energy of the wheelset during its motion along a tangent track. This contribution is explicitly detailed in Eq. (24) of [15]. Considering the new terms due to the curve, the element matrices in Eq. (9) are given by the following expressions:

$$\begin{aligned}
\mathbf{P}^e &= \int_{V^e} \rho \mathbf{N}^T \tilde{\boldsymbol{\omega}} \mathbf{N} dV, \\
\mathbf{S}^e &= \int_{V^e} \rho \mathbf{N}^T \tilde{\boldsymbol{\omega}} \left(\frac{\partial \mathbf{N}}{\partial \theta} + \mathbf{J} \mathbf{N} \right) dV, \\
\mathbf{R}^e &= \int_{V^e} \rho \mathbf{N}^T \dot{\tilde{\boldsymbol{\omega}}} \mathbf{N} dV, \\
\mathbf{B}^e &= - \int_{V^e} \rho \mathbf{N}^T \tilde{\boldsymbol{\omega}}^T \tilde{\boldsymbol{\omega}} \mathbf{N} dV, \\
\mathbf{U}^e &= - \int_{V^e} \rho \mathbf{N}^T \tilde{\boldsymbol{\omega}} \hat{\mathbf{e}}_2 r dV, \\
\mathbf{H}^e &= - \int_{V^e} \rho \mathbf{N}^T \dot{\tilde{\boldsymbol{\omega}}} \mathbf{u} dV, \\
\mathbf{L}^e &= \int_{V^e} \rho \mathbf{N}^T \tilde{\boldsymbol{\omega}}^T \tilde{\boldsymbol{\omega}} \mathbf{u} dV, \\
\mathbf{G}^e &= - \int_{V^e} \rho \mathbf{N}^T \boldsymbol{\Theta}^T dV,
\end{aligned} \tag{10}$$

where V^e is the volume of the e th element, $\tilde{\boldsymbol{\omega}} = \boldsymbol{\Theta}^T \tilde{\boldsymbol{\omega}}_c \boldsymbol{\Theta}$ represents the angular velocity matrix of the track frames formulated in the cylindrical reference system, the matrix \mathbf{J} is given in Appendix A and $\hat{\mathbf{e}}_2 = (0 \ 1 \ 0)^T$. The terms of the Lagrange equations associated with the wheelset potential energy (related to the stiffness matrix \mathbf{K}) are equal to those for a tangent track and can be found in Eqs. (19) and (24) of [15]. Assembling the element matrices into the global ones according to the FEM approach [23] and considering the contribution of both the last term in Eq. (9) and the elastic potential energy, the equations of motion (EoM) of the wheelset when running on a curved track are given by:

$$\begin{aligned}
\mathbf{M} \ddot{\mathbf{w}}(t) + (2\Omega \mathbf{V} + 2\mathbf{P}) \dot{\mathbf{w}}(t) + (\mathbf{K} + \Omega^2 \mathbf{A} + 2\Omega \mathbf{S} + \mathbf{R} + \mathbf{B}) \mathbf{w}(t) \\
= \Omega^2 \mathbf{c} + 2\Omega \mathbf{U} + \mathbf{H} + \mathbf{L} + \mathbf{G} \mathbf{T}^T \ddot{\mathbf{p}}_0 + \mathcal{F}(t),
\end{aligned} \tag{11}$$

where the matrices \mathbf{M} , \mathbf{V} , \mathbf{K} , \mathbf{A} , and \mathbf{c} describe the behaviour of the wheelset on a tangent track, the expressions for which can be found in Eq. (25) of [15]. The force vector \mathcal{F} accounts for the external forces applied to the system due to the wheel/rail interaction. In order to evaluate the rolling noise radiated by the wheels in the wheelset, the model is transformed to the frequency domain, in which the EoM can be expressed for $\omega > 0$ as:

$$(-\omega^2 \mathbf{M} + i\omega (2\Omega \mathbf{V} + 2\mathbf{P}) + \mathbf{K} + \Omega^2 \mathbf{A} + 2\Omega \mathbf{S} + \mathbf{R} + \mathbf{B}) \mathbf{w}(\omega) = \mathcal{F}(\omega). \tag{12}$$

Regarding the sound radiation from the wheelset, the acoustic model developed by Thompson [19] is applied on the surface vibrational field of both wheels, while the axle radiation is considered to be insignificant compared with that of the wheels.

3. Axisymmetric dynamic model of the wheelset

Due to the axial symmetry of the wheelset geometry, the displacement field can be represented using a Fourier series expansion around the circumferential direction as follows [24]:

$$\begin{aligned}
w_r &= w_{r,0} + \sum_{n>0} (w_{r,n} \cos(n\theta) - \bar{w}_{r,n} \sin(n\theta)), \\
w_\theta &= -\bar{w}_{\theta,0} + \sum_{n>0} (w_{\theta,n} \sin(n\theta) - \bar{w}_{\theta,n} \cos(n\theta)), \\
w_z &= w_{z,0} + \sum_{n>0} (w_{z,n} \cos(n\theta) - \bar{w}_{z,n} \sin(n\theta)),
\end{aligned} \tag{13}$$

with n being an integer number representing each Fourier term. For convenience, the harmonic amplitudes can be assembled in a vector \mathbf{w}_h , defined by:

$$\begin{aligned}
\mathbf{w}_h &= (\mathbf{w}_0 \quad \mathbf{w}_1 \quad \cdots \quad \mathbf{w}_n \quad \cdots \quad \mathbf{w}_m)^\top, \\
\mathbf{w}_0 &= (w_{r,0} \quad w_{z,0} \quad \bar{w}_{\theta,0}), \\
\mathbf{w}_n &= (w_{r,n} \quad w_{\theta,n} \quad w_{z,n} \quad \bar{w}_{r,n} \quad \bar{w}_{\theta,n} \quad \bar{w}_{z,n}), \quad n = 1, \dots, m,
\end{aligned} \tag{14}$$

where a truncation up to the Fourier term m is assumed on the expansion of the wheelset response. When considering this expansion, the kinetic energy of the wheelset described in Eq. (7) can be integrated analytically over the θ coordinate, as detailed in Appendix B. Unlike the tangent track case [15], the harmonics from different Fourier terms are now coupled. The integration mentioned above yields the following expression for the kinetic energy:

$$\begin{aligned}
K &= \frac{1}{2} \dot{\mathbf{p}}_c^\top \dot{\mathbf{p}}_c M + \pi \dot{\mathbf{p}}_c^\top \tilde{\boldsymbol{\omega}}_c \int_A \rho (\mathbf{J}_1 \mathbf{w}_h + \mathbf{J}_2) r dA + \pi \dot{\mathbf{p}}_c^\top \int_A \rho \mathbf{J}_1 \dot{\mathbf{w}}_h r dA \\
&+ \frac{\pi}{2} \int_A \rho ((\omega_{11}^2 + \omega_{33}^2) r^2 + 2\omega_{22}^2 z^2) r dA + \pi \int_A \rho \mathbf{J}_3^\top \mathbf{w}_h r dA + \frac{\pi}{2} \int_A \rho \mathbf{w}_h^\top \mathbf{J}_4 \mathbf{w}_h r dA \\
&+ \Omega 2\pi \omega_2 \int_A \rho r^3 dA + \pi \int_A \rho (\mathbf{J}_5^\top + \mathbf{w}_h^\top \mathbf{J}_7) \dot{\mathbf{w}}_h r dA + \Omega \pi \int_A \rho (\mathbf{J}_6^\top + \mathbf{w}_h^\top \mathbf{J}_8) \mathbf{w}_h r dA \\
&+ K_t,
\end{aligned} \tag{15}$$

where A is the area of the wheelset cross-section, $dA = dr dz$, and the matrices \mathbf{J}_i are given in Appendix A. The kinetic energy of the wheelset associated with a tangent track, K_t , is given in Eqs. (36) and (37) of reference [15]; equivalently, it can be expressed as a function of the assembled vector \mathbf{w}_h as indicated in Appendix B. Regarding the angular velocities of the track frame ω_i as well as the squared angular velocities ω_{ij}^2 , these can be identified from the following terms in $\tilde{\boldsymbol{\omega}}_c$ and $\tilde{\boldsymbol{\omega}}_c^\top \tilde{\boldsymbol{\omega}}_c$:

$$\tilde{\boldsymbol{\omega}}_c = \begin{bmatrix} 0 & -\omega_3 & \omega_2 \\ \omega_3 & 0 & -\omega_1 \\ -\omega_2 & \omega_1 & 0 \end{bmatrix}, \quad \tilde{\boldsymbol{\omega}}_c^\top \tilde{\boldsymbol{\omega}}_c = \begin{bmatrix} \omega_{11}^2 & \omega_{12}^2 & \omega_{13}^2 \\ \omega_{12}^2 & \omega_{22}^2 & \omega_{23}^2 \\ \omega_{13}^2 & \omega_{23}^2 & \omega_{33}^2 \end{bmatrix}, \quad \begin{aligned} \omega_1 &= 0, \\ \omega_2 &= \dot{\beta} \sin \gamma, \\ \omega_3 &= \dot{\beta} \cos \gamma, \end{aligned} \tag{16}$$

where $\dot{\beta} = \frac{V_v}{R_c}$ for a left-hand curve and $\dot{\beta} = -\frac{V_v}{R_c}$ for a right-hand curve, V_v being the vehicle speed and R_c the curve radius. An axisymmetric FE model is proposed for the wheelset cross-section (see Fig. 2), which allows the evaluation of the unknown harmonic amplitudes by means of the following interpolation in the e th element of the mesh:

$$\mathbf{w}_h(r, z, t) = \mathbf{N}_h(r, z) \mathbf{w}_h^e(t), \tag{17}$$

\mathbf{N}_h being the shape function matrix defined for the axisymmetric model. When p nodes are considered in the e th element, this matrix is given by:

$$\mathbf{N}_h = [\mathbf{N}_{h,1} \quad \cdots \quad \mathbf{N}_{h,j} \quad \cdots \quad \mathbf{N}_{h,p}], \quad \mathbf{N}_{h,j} = N_j \mathbf{I}_{(3+6m) \times (3+6m)}, \quad (18)$$

where N_j is the shape function associated with the j th node and $\mathbf{I}_{k \times k}$ is the identity matrix of order k . The vector of harmonic amplitudes of the e th element \mathbf{w}_h^e can be expressed as follows:

$$\begin{aligned} \mathbf{w}_h^e &= (\mathbf{w}_{h,1}^e \quad \cdots \quad \mathbf{w}_{h,j}^e \quad \cdots \quad \mathbf{w}_{h,p}^e)^T, \\ \mathbf{w}_{h,j}^e &= (\mathbf{w}_{0,j}^e \quad \mathbf{w}_{1,j}^e \quad \cdots \quad \mathbf{w}_{n,j}^e \quad \cdots \quad \mathbf{w}_{m,j}^e), \end{aligned} \quad (19)$$

where $\mathbf{w}_{0,j}^e$ contains the three harmonic amplitudes in the j th node defined for $n = 0$ and $\mathbf{w}_{n,j}^e$ the six harmonic amplitudes in the same node defined for $n > 0$, sorted as expressed in Eq. (14).

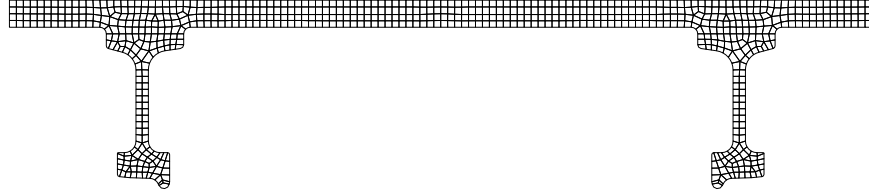


Fig. 2: Axisymmetric FE mesh of the wheelset cross-section.

When considering the kinetic energy in Eq. (15) for the e th element and evaluating the Lagrange equations, the result is given by:

$$\begin{aligned} \frac{D}{Dt} \left(\frac{\partial K}{\partial \dot{\mathbf{w}}_h^e} \right)^T - \left(\frac{\partial K}{\partial \mathbf{w}_h^e} \right)^T &= 2\mathbf{P}_h^e \dot{\mathbf{w}}_h^e + (2\Omega \mathbf{S}_h^e + \mathbf{R}_h^e + \mathbf{B}_h^e) \mathbf{w}_h^e - 2\Omega \mathbf{U}_h^e - \mathbf{H}_h^e - \mathbf{L}_h^e \\ &\quad - \mathbf{G}_h^e \mathbf{T}^T \ddot{\mathbf{p}}_0 + \left(\frac{D}{Dt} \left(\frac{\partial K_t}{\partial \dot{\mathbf{w}}_h^e} \right)^T - \left(\frac{\partial K_t}{\partial \mathbf{w}_h^e} \right)^T \right), \end{aligned} \quad (20)$$

where, as in the 3D model, the last term considers the contribution of the wheelset kinetic energy during its motion along a tangent track. The development of this term can be found in Eqs. (53) and (60) of reference [15], wherein the harmonics are uncoupled, allowing the matrices to be expressed independently for each Fourier term. Later these matrices will be reformulated for the assembled vector of harmonic amplitudes. The element matrices for the new terms arising from Eq. (20) are obtained using the following expressions:

$$\begin{aligned}
\mathbf{P}_h^e &= \sum_{i=1}^3 \omega_i \mathbf{P}_{h,i}^e, & \mathbf{P}_{h,i}^e &= \pi \int_{A^e} \rho \mathbf{N}_h^T \frac{\partial \mathbf{J}_7^T}{\partial \omega_i} \mathbf{N}_h r dA, \\
\mathbf{S}_h^e &= \sum_{i=1}^3 \omega_i \mathbf{S}_{h,i}^e, & \mathbf{S}_{h,i}^e &= -\frac{\pi}{2} \int_{A^e} \rho \mathbf{N}_h^T \left(\frac{\partial \mathbf{J}_8^T}{\partial \omega_i} + \frac{\partial \mathbf{J}_8}{\partial \omega_i} \right) \mathbf{N}_h r dA, \\
\mathbf{R}_h^e &= \sum_{i=1}^3 \dot{\omega}_i \mathbf{R}_{h,i}^e, & \mathbf{R}_{h,i}^e &= \mathbf{P}_{h,i}^e, \\
\mathbf{B}_h^e &= \sum_{i=1}^3 \sum_{j=i}^3 \omega_{ij}^2 \mathbf{B}_{h,ij}^e, & \mathbf{B}_{h,ij}^e &= -\frac{\pi}{2} \int_{A^e} \rho \mathbf{N}_h^T \left(\frac{\partial \mathbf{J}_4^T}{\partial \omega_{ij}^2} + \frac{\partial \mathbf{J}_4}{\partial \omega_{ij}^2} \right) \mathbf{N}_h r dA, \\
\mathbf{U}_h^e &= \sum_{i=1}^3 \omega_i \mathbf{U}_{h,i}^e, & \mathbf{U}_{h,i}^e &= \frac{\pi}{2} \int_{A^e} \rho \mathbf{N}_h^T \frac{\partial \mathbf{J}_6}{\partial \omega_i} r dA, \\
\mathbf{H}_h^e &= \sum_{i=1}^3 \dot{\omega}_i \mathbf{H}_{h,i}^e, & \mathbf{H}_{h,i}^e &= -\pi \int_{A^e} \rho \mathbf{N}_h^T \frac{\partial \mathbf{J}_5}{\partial \omega_i} r dA, \\
\mathbf{L}_h^e &= \sum_{i=1}^3 \sum_{j=i}^3 \omega_{ij}^2 \mathbf{L}_{h,ij}^e, & \mathbf{L}_{h,ij}^e &= \pi \int_{A^e} \rho \mathbf{N}_h^T \frac{\partial \mathbf{J}_3}{\partial \omega_{ij}^2} r dA, \\
\mathbf{G}_h^e &= -\pi \int_{A^e} \rho \mathbf{N}_h^T \mathbf{J}_1^T r dA,
\end{aligned} \tag{21}$$

where A^e is the area of the e th element. Regarding the elastic potential energy and its contribution to the Lagrange equations, the expressions are the same as for the case of a wheelset on a tangent track (see [15]). Following the FEM approach, the element matrices in Eq. (21) are assembled into the global ones and, together with the contribution from both the last term in Eq. (20) and the potential energy, the EoM of the wheelset using an axisymmetric approach are given by:

$$\begin{aligned}
& \mathbf{M}_h \ddot{\mathbf{w}}_h(t) + \left(2\Omega \mathbf{V}_h + 2 \sum_{i=1}^3 \omega_i \mathbf{P}_{h,i} \right) \dot{\mathbf{w}}_h(t) \\
& + \left(\mathbf{K}_h + \Omega^2 \mathbf{A}_h + 2\Omega \sum_{i=1}^3 \omega_i \mathbf{S}_{h,i} + \sum_{i=1}^3 \dot{\omega}_i \mathbf{R}_{h,i} + \sum_{i=1}^3 \sum_{j=i}^3 \omega_{ij}^2 \mathbf{B}_{h,ij} \right) \mathbf{w}_h(t) \\
& = \Omega^2 \mathbf{c}_h + 2\Omega \sum_{i=1}^3 \omega_i \mathbf{U}_{h,i} + \sum_{i=1}^3 \dot{\omega}_i \mathbf{H}_{h,i} + \sum_{i=1}^3 \sum_{j=i}^3 \omega_{ij}^2 \mathbf{L}_{h,ij} + \mathbf{G}_h \mathbf{T}^T \ddot{\mathbf{p}}_0 + \mathfrak{F}_h(t).
\end{aligned} \tag{22}$$

It is worth noting that, in the proposed approach, the angular velocities appear explicitly in the EoM, while the matrices are functions only of the coordinates r and z . This does not happen for the 3D model, associated with Eq. (11), in which the angular velocities are included implicitly in the EoM through the definition of the matrices involved; however, these matrices could as well be formulated to be independent of those variables if the matrix multiplications in the integrals of Eq. (10) are developed. By doing this, it is not necessary to evaluate the matrices of the wheelset at every time step of a curving simulation even if

the curve radius, vehicle velocity or superelevation (cant) are not constant (note that these three quantities define the aforementioned angular velocities).

Regarding the force vector \mathcal{F}_h in Eq. (22), it considers the wheel/rail interaction forces after expanding them in Fourier series; a detailed methodology to evaluate the harmonic amplitudes of the forces for each Fourier term is exposed in Section 4.3 of [15]. The vector \mathcal{F}_h is then obtained by assembling the amplitudes from each Fourier term in accordance with the order of the vector of unknowns \mathbf{w}_h , defined in Eq. (14). The matrices \mathbf{M}_h , \mathbf{V}_h , \mathbf{K}_h , \mathbf{A}_h , and \mathbf{c}_h describe the dynamics of the wheelset when running on a tangent track and their expressions can be found in Eqs. (54) and (61) of reference [15], formulated independently for each Fourier term. Due to the coupling between harmonics introduced by the new matrices in a curved track, the matrices from [15] could be assembled according to \mathbf{w}_h . Alternatively, the assembled element matrices can be evaluated as follows:

$$\begin{aligned}
\mathbf{M}_h^e &= \pi \int_{A^e} \rho \mathbf{N}_h^T \mathbf{J}_9 \mathbf{N}_h r dA, \\
\mathbf{V}_h^e &= \pi \int_{A^e} \rho \mathbf{N}_h^T \mathbf{J}_{11}^T \mathbf{N}_h r dA, \\
\mathbf{K}_h^e &= \pi \int_{A^e} \tilde{\mathbf{B}}^T \tilde{\mathbf{D}} \tilde{\mathbf{B}} r dA, \\
\mathbf{A}_h^e &= -\pi \int_{A^e} \rho \mathbf{N}_h^T (\mathbf{J}_{13}^T + \mathbf{J}_{13}) \mathbf{N}_h r dA, \\
\mathbf{c}_h^e &= \pi \int_{A^e} \rho \mathbf{N}_h^T \mathbf{J}_{10} r dA,
\end{aligned} \tag{23}$$

where $\tilde{\mathbf{B}} = \tilde{\mathbf{L}} \mathbf{N}_h$, with $\tilde{\mathbf{L}}$ being a matrix operator given in Appendix A together with the matrix $\tilde{\mathbf{D}}$. As in the 3D model, to allow the subsequent sound radiation evaluation, the EoM are transformed to the frequency domain for $\omega > 0$, yielding:

$$\begin{aligned}
&\left(-\omega^2 \mathbf{M}_h + i\omega \left(2\Omega \mathbf{V}_h + 2 \sum_{i=1}^3 \omega_i \mathbf{P}_{h,i} \right) + \mathbf{K}_h + \Omega^2 \mathbf{A}_h + 2\Omega \sum_{i=1}^3 \omega_i \mathbf{S}_{h,i} + \sum_{i=1}^3 \dot{\omega}_i \mathbf{R}_{h,i} \right. \\
&\quad \left. + \sum_{i=1}^3 \sum_{j=i}^3 \omega_{ij}^2 \mathbf{B}_{h,ij} \right) \mathbf{w}_h(\omega) = \mathcal{F}_h(\omega).
\end{aligned} \tag{24}$$

In line with the dynamic behaviour of the wheelset, the sound radiation can be formulated in a two-dimensional frame, taking advantage of the expansion of the response around the circumferential direction. To this end, the methodology described in Section 4.5 of reference [15] is performed over the surface of the wheels. However, the RBM contribution mentioned in the previous reference is explicitly excluded in this work since the wheelset FE model proposed already includes it. As stated in Section 2, the axle contribution to the acoustic radiation is neglected.

4. Vehicle/track interaction model

In this work, the Manchester Benchmark vehicle [25] is considered to be running in coasting condition on a curved track with constant curvature. The behaviour of the wheelset

and track in a curve is characterized as a superposition of the steady-state regime and the dynamic oscillations around it. For simplicity, the former is obtained using the VI-Rail software [16]. The steady-state variables on the curve, together with the wheel and rail combined roughness spectrum, are used as an input for the calculation of rolling noise radiated by the wheelset and track. The vibroacoustic behaviour of the wheelset is described by the models previously developed; a modal damping ratio ξ is included in the wheelset model using the empirical relation proposed by Thompson [4], relating the modal damping ratio and the number of nodal diameters of a modeshape. The track behaviour and the wheel/rail interaction problem are addressed as described below.

4.1. Track

The two-layer continuous track model described in [26] is adapted for the current investigation by including both rails, which are dynamically coupled through the sleepers. This allows both the dynamic and acoustic behaviour of the rails and sleepers to be evaluated. The sound radiation calculation requires the assumption that the different waves in the track can be considered to radiate independently [20], and a condition for this to be true is that different waves have different wavenumbers. Due to the symmetry of the track, for each wavenumber there are two independent waves (symmetric and antisymmetric relative to the track centre) and so the previous assumption does not hold. To apply the acoustic model, these pairs of waves are combined and thus their contribution to the track response \mathbf{w}_T can be expressed as follows:

$$\begin{aligned} \mathbf{w}_T &= \sum_r (A_r \boldsymbol{\Psi}_r + \bar{A}_r \bar{\boldsymbol{\Psi}}_r) e^{-ik_r|x|} = \sum_r \tilde{A}_r \tilde{\boldsymbol{\Psi}}_r e^{-ik_r|x|}, \\ \tilde{A}_r &= A_r, \\ \tilde{\boldsymbol{\Psi}}_r &= \boldsymbol{\Psi}_r + \frac{\bar{A}_r}{A_r} \bar{\boldsymbol{\Psi}}_r, \end{aligned} \tag{25}$$

where subscript r represents each pair of waves with the same wavenumber, x is the longitudinal coordinate of the track coordinate system (running direction), and A_r , $\boldsymbol{\Psi}_r$, and k_r represent, respectively, the generalized coordinate, waveshape and wavenumber of the corresponding wave. The generalized coordinates and waveshapes with and without a bar are associated with the two independent waves, while the ones with a tilde represent the combined wave properties. In references [17, 18], a detailed explanation on how to evaluate the waveshapes and wavenumbers is given. Regarding the generalized coordinates, they depend on the external forces applied to the track, and given these forces, the coordinates can be evaluated as described in [20]. These wave properties are subsequently used in the acoustic model, which predicts both rail and sleeper sound power radiation. In this work, due to the existence of significant lateral forces coming from the curving behaviour, the sleeper is assumed to radiate from top, bottom, and both lateral faces, and it is modelled as a rigid body with 4 degrees of freedom (DoF): three Cartesian translations and a rotation with respect to the longitudinal axis (running direction). While the bottom surface of the sleeper is covered by the ballast, the study in this work is limited to the radiated sound power and therefore the contribution of the bottom surface is also considered.

Note that, according to reference [27], the curvature of the track does not notably affect its dynamic response when the curve radius is greater than 30 m, a value lower than the

minimum radius used in the simulations conducted in this work. Therefore, the curvature is not considered in the track dynamic model described above.

4.2. Wheel/rail interaction

Rolling noise occurs as a consequence of the wheel/rail interaction when roughness is present on their rolling surfaces. The forces resulting from this interaction are evaluated using the model developed by Thompson [4, 28], which is here extended to consider non-zero mean values of the creepages, the dynamic fluctuation of the normal contact force and the effect of the contact angle, leading to a coupling of vertical and lateral vibration of the wheels and rails. The wheel/rail interaction module is defined in the form of a linearized input-output relationship between the relative motion of the wheel and rail surfaces at the contact point and the contact forces. This relationship is initially derived for the case of a wheelset running centred over the track so that the small contact angle can be neglected. Then, the model is extended to the case of a wheelset running through a curve, considering the effect of the contact angle, i.e. the inclination of the plane tangent to the contacting surfaces with respect to the top-of-rail plane.

Considering the three directions of the space, a diagram of the interaction model showing the sign convention used in this work is depicted in Fig. 3. The Roman numerals I and II make reference to the left and right sides, respectively, while longitudinal, lateral, and vertical directions are denoted by the Arabic numerals 1, 2, and 3, respectively. The text I/II indicates that the same diagram applies to both sides. Roughness is assumed to exist only in the vertical direction, in which the wheel and rail are connected through a contact stiffness (see Fig. 3(c)). In the other two directions, the relation between velocity and force in the contact area will be explored later. Due to continuity in the contact, the following relation between velocities is found [4]:

$$\begin{pmatrix} v_{W,I1} \\ v_{W,I2} \\ v_{W,I3} \\ v_{W,II1} \\ v_{W,II2} \\ v_{W,II3} \end{pmatrix} - \begin{pmatrix} v_{R,I1} \\ v_{R,I2} \\ v_{R,I3} \\ v_{R,II1} \\ v_{R,II2} \\ v_{R,II3} \end{pmatrix} - \begin{pmatrix} v_{C,I1} \\ v_{C,I2} \\ v_{C,I3} \\ v_{C,II1} \\ v_{C,II2} \\ v_{C,II3} \end{pmatrix} = \begin{pmatrix} 0 \\ 0 \\ r_{S,I} \\ 0 \\ 0 \\ r_{S,II} \end{pmatrix} i\omega \implies \mathbf{v}_W - \mathbf{v}_R - \mathbf{v}_C = \mathbf{r}i\omega, \quad (26)$$

where, in the velocities, the first subscript refers to the component (W for wheelset, R for rail, and C for contact) and the second to the element side and direction (for example, $v_{R,I2}$ is the lateral velocity of the left rail contact point). A wheel/rail combined (system) roughness with angular frequency ω is considered in the vertical direction of the left and right sides with amplitude $r_{S,I}$ and $r_{S,II}$, respectively, which are assumed to be randomly uncorrelated. Note that, while the subscript c is used in Sections 2 and 3 to denote the travelling Cartesian frame, the subscript C (capital letter) is employed in this section to denote a contact variable. For convenience, the first vector in the left hand side of Eq. (26) is defined as \mathbf{v}_W , the second as \mathbf{v}_R , and the third as \mathbf{v}_C , while the vector in the right hand is defined as \mathbf{r} . Assembling the interaction forces accordingly, that is $\mathbf{F} = (F_{I1} \ F_{I2} \ F_{I3} \ F_{II1} \ F_{II2} \ F_{II3})^T$, and taking into account the sign convention shown in Fig. 3, the wheelset velocities can be related to the forces as follows:

$$\mathbf{v}_W = - \begin{bmatrix} Y_{W,I1-I1} & Y_{W,I1-I2} & Y_{W,I1-I3} & Y_{W,I1-II1} & Y_{W,I1-II2} & Y_{W,I1-II3} \\ Y_{W,I2-I1} & Y_{W,I2-I2} & Y_{W,I2-I3} & Y_{W,I2-II1} & Y_{W,I2-II2} & Y_{W,I2-II3} \\ Y_{W,I3-I1} & Y_{W,I3-I2} & Y_{W,I3-I3} & Y_{W,I3-II1} & Y_{W,I3-II2} & Y_{W,I3-II3} \\ Y_{W,II1-I1} & Y_{W,II1-I2} & Y_{W,II1-I3} & Y_{W,II1-II1} & Y_{W,II1-II2} & Y_{W,II1-II3} \\ Y_{W,II2-I1} & Y_{W,II2-I2} & Y_{W,II2-I3} & Y_{W,II2-II1} & Y_{W,II2-II2} & Y_{W,II2-II3} \\ Y_{W,II3-I1} & Y_{W,II3-I2} & Y_{W,II3-I3} & Y_{W,II3-II1} & Y_{W,II3-II2} & Y_{W,II3-II3} \end{bmatrix} \mathbf{F} = -\mathbf{Y}_W \mathbf{F}, \quad (27)$$

with \mathbf{Y}_W being a mobility matrix associated with the wheelset contact points. As for the velocities, the first subscript of the mobilities refers to the element while the second subscript denotes where the response is measured and the unit force applied. For example, the mobility $Y_{W,II3-I2}$ represents the vertical (3) velocity of the wheelset right side contact point (II) when only a unit lateral (2) force is applied on the wheelset left side contact point (I). These mobilities are determined using either the three-dimensional or axisymmetric wheelset model proposed in this work. Equivalently, the rail velocities are given by:

$$\mathbf{v}_R = \mathbf{Y}_R \mathbf{F}, \quad (28)$$

where the rail mobility matrix is defined analogously as the one for the wheel. Using the model discussed in Section 4.1, the components of \mathbf{Y}_R are determined by applying a unit force and solving the generalized coordinates [20], and then evaluating Eq. (25) and its time derivative. Regarding the contact velocities, the following relation with the interaction forces is found:

$$\mathbf{v}_C = \begin{bmatrix} Y_{C,I1-I1} & 0 & Y_{C,I1-I3} & 0 & 0 & 0 \\ 0 & Y_{C,I2-I2} & Y_{C,I2-I3} & 0 & 0 & 0 \\ 0 & 0 & Y_{C,I3-I3} & 0 & 0 & 0 \\ 0 & 0 & 0 & Y_{C,II1-II1} & 0 & Y_{C,II1-II3} \\ 0 & 0 & 0 & 0 & Y_{C,II2-II2} & Y_{C,II2-II3} \\ 0 & 0 & 0 & 0 & 0 & Y_{C,II3-II3} \end{bmatrix} \mathbf{F} = \mathbf{Y}_C \mathbf{F}, \quad (29)$$

where the left and right contact zones are not coupled. Thus, hereafter the side subscripts I and II are omitted for simplicity. A Hertz contact spring is considered for the normal direction, in which the (linearized) mobility is given by [4, 28]:

$$Y_{C,3-3} = i\omega \frac{\xi}{2} \left(\frac{2}{3E'^2 F_3^0 r_e} \right)^{\frac{1}{3}}, \quad (30)$$

with $E' = \frac{E}{1-\nu^2}$ being the plane strain elastic modulus, E and ν the Young's modulus and Poisson's ratio, respectively, F_3^0 the steady-state (superscript 0) force normal to the contact, r_e the effective radius of curvature of the wheel/rail surfaces in contact, and ξ a parameter depending on the aspect ratio of the assumed contact patch ellipse. Further details on the last two parameters can be found in [4]. It is worth indicating that the mobility in Eq. (30) is linearized about the steady-state normal load obtained from the curve simulations conducted in the VI-Rail software [16]. In relation to the tangential directions, the model developed by Gross-Thebing [29] is utilized, which considers non-zero steady-state values of longitudinal, lateral, and spin creepages to evaluate the dynamic tangent forces at the

contact. In the aforementioned work, the creepages are described as a superposition of a mean value (steady-state value) and a fluctuation around it:

$$\begin{aligned}\gamma_1 &= \gamma_1^0 + \Delta\gamma_1 = \frac{1}{V_v} (v_{C,1}^0 + \Delta v_{C,1}), \\ \gamma_2 &= \gamma_2^0 + \Delta\gamma_2 = \frac{1}{V_v} (v_{C,2}^0 + \Delta v_{C,2}), \\ w_3 &= w_3^0 + \Delta w_3 = \frac{1}{V_v} (\omega_{C,3}^0 + \Delta\omega_{C,3}),\end{aligned}\tag{31}$$

where γ_1 , γ_2 , and w_3 are the longitudinal, lateral, and spin creepages, respectively, $\omega_{C,3}$ is the relative rotational speed between the wheel and rail contact points around the normal axis to the contact patch, subscript 0 represents the mean value and Δ denotes the increment around the previous value. Considering only linearized effects, the creep forces are related to the creepages as follows [29]:

$$\begin{aligned}F_1 &= F_1^0 + Gab\widehat{C}_{11}\Delta\gamma_1, \\ F_2 &= F_2^0 + Gab\left(\widehat{C}_{22}\Delta\gamma_2 + \sqrt{ab}\widehat{C}_{23}\Delta w_3\right), \\ M_3 &= M_3^0 + Gab\left(\sqrt{ab}\widehat{C}_{32}\Delta\gamma_2 + ab\widehat{C}_{33}\Delta w_3\right),\end{aligned}\tag{32}$$

with G being the shear modulus, a and b the longitudinal (running direction) and lateral semi-axis lengths of the contact patch (assumed elliptical), respectively, \widehat{C}_{jk} the complex creep coefficients developed by Gross-Thebing [29], which depend on the frequency and steady-state values of the creepages, and M_3 the creep torque around the normal direction. As pointed out by Thompson [30, 31], the normal load F_3 influences the contact patch size and, in this case, also the complex creep coefficients and steady-state creep forces. Taking increments in Eq. (32) and neglecting the products of small quantities, the following equations are obtained:

$$\begin{aligned}\Delta F_1 &= \Delta F_1^0 + \frac{G}{V_v} a^0 b^0 \widehat{C}_{11}^0 \Delta v_{C,1}, \\ \Delta F_2 &= \Delta F_2^0 + \frac{G}{V_v} a^0 b^0 \left(\widehat{C}_{22}^0 \Delta v_{C,2} + \sqrt{a^0 b^0} \widehat{C}_{23}^0 \Delta\omega_{C,3} \right), \\ \Delta M_3 &= \Delta M_3^0 + \frac{G}{V_v} a^0 b^0 \left(\sqrt{a^0 b^0} \widehat{C}_{32}^0 \Delta v_{C,2} + a^0 b^0 \widehat{C}_{33}^0 \Delta\omega_{C,3} \right).\end{aligned}\tag{33}$$

Since the steady-state creep forces are dependent on the contact patch semi-axis lengths as well as the normal load [32], their increments can be expressed as follows:

$$\Delta F_k^0 = \frac{\partial F_k^0}{\partial a} \Delta a + \frac{\partial F_k^0}{\partial b} \Delta b + \frac{\partial F_k^0}{\partial F_3} \Delta F_3, \quad k = 1, 2, 6, \quad F_6^0 = M_3^0,\tag{34}$$

in which subscript 6 makes reference to the rotational velocity and torque around the direction 3 (normal to the contact patch, i.e. spin). The semi-axis lengths of the contact patch are given by [4]:

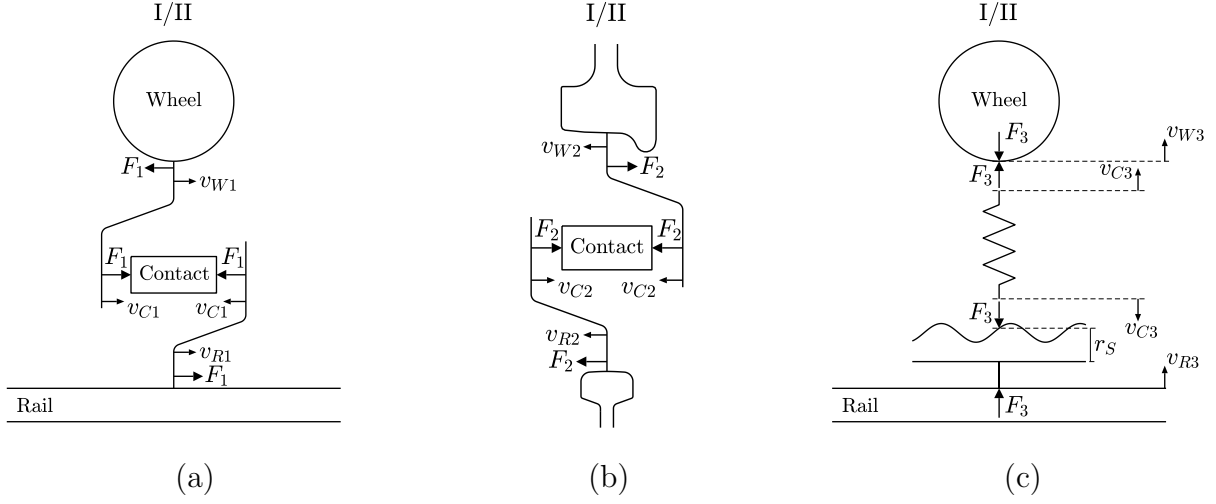


Fig. 3: Diagram of the wheel/rail interaction model. (a) Longitudinal direction. (b) Lateral direction. (c) Vertical direction.

$$\begin{aligned}
 a &= \sigma_1 \left(\frac{3F_3 r_e}{2E'} \right)^{\frac{1}{3}}, \\
 b &= \sigma_2 \left(\frac{3F_3 r_e}{2E'} \right)^{\frac{1}{3}},
 \end{aligned} \tag{35}$$

where σ_1 and σ_2 are parameters depending on the aspect ratio of the contact patch ellipse (the corresponding expressions can be found in [4]). Therefore, the increments of these lengths can be evaluated as follows:

$$\begin{aligned}
 \Delta a &= \frac{\partial a}{\partial F_3} \Delta F_3 = \frac{a}{3F_3} \Delta F_3, \\
 \Delta b &= \frac{\partial b}{\partial F_3} \Delta F_3 = \frac{b}{3F_3} \Delta F_3.
 \end{aligned} \tag{36}$$

Introducing Eqs. (34) and (36) into Eq. (33), the increments of the contact relative velocities are related to those of the creep forces by:

$$\begin{aligned}
 \frac{G}{V_v} a^0 b^0 \widehat{C}_{11}^0 \Delta v_{C,1} &= \Delta F_1 - T_1 \Delta F_3, \\
 \frac{G}{V_v} a^0 b^0 \widehat{C}_{22}^0 \Delta v_{C,2} + \frac{G}{V_v} (a^0 b^0)^{\frac{3}{2}} \widehat{C}_{23}^0 \Delta \omega_{C,3} &= \Delta F_2 - T_2 \Delta F_3, \\
 \frac{G}{V_v} (a^0 b^0)^{\frac{3}{2}} \widehat{C}_{32}^0 \Delta v_{C,2} + \frac{G}{V_v} (a^0 b^0)^2 \widehat{C}_{33}^0 \Delta \omega_{C,3} &= \Delta M_3 - T_6 \Delta F_3,
 \end{aligned} \tag{37}$$

where the variables T_k are given by:

$$T_k = \frac{\partial F_k^0}{\partial a} \frac{a}{3F_3} + \frac{\partial F_k^0}{\partial b} \frac{b}{3F_3} + \frac{\partial F_k^0}{\partial F_3}, \quad k = 1, 2, 6, \quad F_6^0 = M_3^0, \tag{38}$$

with the partial derivatives of the steady-state forces being, in this work, evaluated numerically using the FASTSIM algorithm developed by Kalker [33] and linearized around the steady-state values. Solving the system in Eq. (37), the contact relative (linear) velocities can be expressed as follows:

$$\begin{aligned} \begin{pmatrix} \Delta v_{C,1} \\ \Delta v_{C,2} \end{pmatrix} &= \begin{bmatrix} \frac{V_v}{Ga^0b^0\widehat{C}_{11}^0} & 0 & -\frac{V_vT_1}{Ga^0b^0\widehat{C}_{11}^0} \\ 0 & \frac{V_v\widehat{C}_{33}^0}{Ga^0b^0S_1} & \frac{V_v(\widehat{C}_{23}^0T_6 - \sqrt{a^0b^0}\widehat{C}_{33}^0T_2)}{G(a^0b^0)^{\frac{3}{2}}S_1} \end{bmatrix} \begin{pmatrix} \Delta F_1 \\ \Delta F_2 \\ \Delta F_3 \end{pmatrix} \\ &= \begin{bmatrix} Y_{C,1-1} & 0 & Y_{C,1-3} \\ 0 & Y_{C,2-2} & Y_{C,2-3} \end{bmatrix} \begin{pmatrix} \Delta F_1 \\ \Delta F_2 \\ \Delta F_3 \end{pmatrix}, \end{aligned} \quad (39)$$

where $S_1 = \widehat{C}_{22}^0\widehat{C}_{33}^0 - \widehat{C}_{23}^0\widehat{C}_{32}^0$. Eq. (39) defines the mobilities $Y_{C,1-1}$, $Y_{C,1-3}$, $Y_{C,2-2}$, and $Y_{C,2-3}$ used in Eq. (29). The coupling between the wheel and rail dynamic spin motion is not considered in this work, but the corresponding mobilities can also be derived from Eq. (37). Note that, as described by Thompson [30, 31], the presence of steady-state creepage (or, equivalently, steady-state creep forces) induces a coupling between the normal and tangential directions, in which a harmonic normal load generates harmonic tangential vibration. The contact mobilities in the previous equation are linearized about the steady-state variables (subscript 0) obtained from the VI-Rail software curve simulations [16]. Finally, by introducing Eqs. (27), (28), and (29) into Eq. (26), the interaction forces are evaluated by solving the resultant system of equations, given by:

$$-(\mathbf{Y}_W + \mathbf{Y}_R + \mathbf{Y}_C)\mathbf{F} = \mathbf{r}\boldsymbol{\omega}, \quad (40)$$

where the wheel and rail combined roughness is considered as an input.

So far, as it is represented in Fig. 3, the components of the wheelset, rail, and contact coordinate systems are considered to be parallel. When the vehicle runs on a curved track, the position of the wheel and rail contact point is displaced, often leading to a non-negligible contact angle. With this consideration, Fig. 4 shows the reference systems of the aforementioned three elements. In this work, the roll angle of the wheelset due to its lateral displacement is assumed to be negligible, so that the wheelset and track frame components are considered to be parallel. The contact reference system is defined rotating the track reference by the contact angle α . The angle γ has already been defined in Section 2 as the cant angle. As the components of the three reference systems are not parallel, Eq. (40) cannot be directly applied. Previously, the mobilities need to be formulated in the same frame. In this work, the interaction is solved in the contact reference system. Therefore, both wheelset and rail mobilities need to be rotated by the contact angle as follows:

$$\begin{aligned} \mathbf{Y}_W^C &= \boldsymbol{\Xi}^T \mathbf{Y}_W^W \boldsymbol{\Xi}, \\ \mathbf{Y}_R^C &= \boldsymbol{\Xi}^T \mathbf{Y}_R^R \boldsymbol{\Xi}, \end{aligned} \quad (41)$$

where the notation for the mobilities has changed by adding a superscript that indicates the frame in which the variable is expressed. Note that \mathbf{Y}_W^W and \mathbf{Y}_R^R are the wheelset and rail mobilities as defined in Eqs. (27) and (28), respectively, where the superscripts are omitted as

the wheel, rail, and contact reference systems are coincident (formulation before considering a non-negligible contact angle). The matrix Ξ is given by:

$$\Xi = \begin{bmatrix} 1 & 0 & 0 & 0 & 0 & 0 \\ 0 & \cos(\alpha_I) & -\sin(\alpha_I) & 0 & 0 & 0 \\ 0 & \sin(\alpha_I) & \cos(\alpha_I) & 0 & 0 & 0 \\ 0 & 0 & 0 & 1 & 0 & 0 \\ 0 & 0 & 0 & 0 & \cos(\alpha_{II}) & -\sin(\alpha_{II}) \\ 0 & 0 & 0 & 0 & \sin(\alpha_{II}) & \cos(\alpha_{II}) \end{bmatrix}, \quad (42)$$

with α_I and α_{II} being the contact angle of the left and right sides, respectively, which are evaluated in the steady-state condition from the steady-state regime calculation performed using software VI-Rail. In order to determine the interaction forces, the matrices \mathbf{Y}_W and \mathbf{Y}_R in Eq. (40) are substituted by \mathbf{Y}_W^C and \mathbf{Y}_R^C , respectively, and the resultant system is solved. Note that the contact mobilities do not need any rotation. The roughness vector \mathbf{r} is also assumed to be expressed in the contact reference system, which means that roughness is only considered in the direction normal to the contact patch. As a result of this methodology, the interaction forces are also expressed in the contact frame.

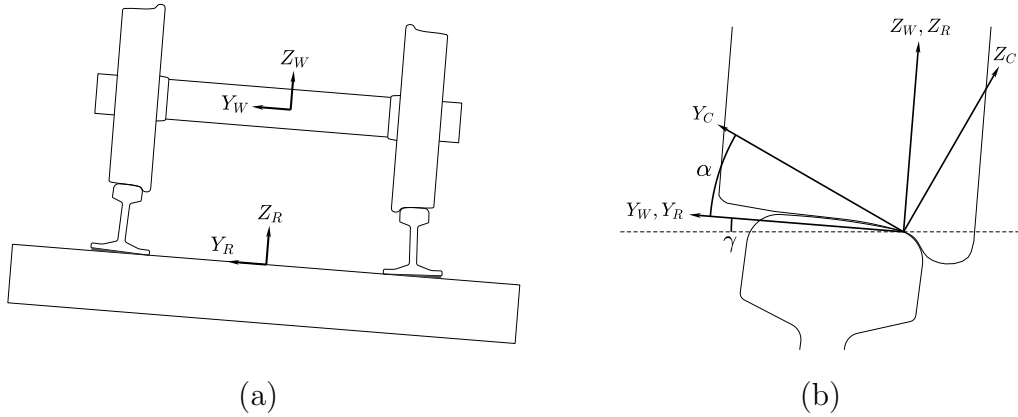


Fig. 4: (a) Diagram of wheelset and rails when running on a curved track along with their reference systems. (b) Zoom around one contact point and angles between the different reference systems.

The combined roughness acting at each wheel/rail contact is considered to be incoherent and so, given a wheelset running on the rails, the methodology to calculate the rolling noise is as follows:

1. The roughness on the right side is set to zero ($r_{S,II} = 0$) and the interaction forces are obtained by solving Eq. (40). Then, the vibrational response to these is evaluated on the surfaces of both wheels, both rails, and sleepers. Subsequently, the rolling noise radiated by these elements is calculated.
2. The same procedure is repeated setting the left side roughness to zero ($r_{S,I} = 0$), resulting in the noise radiated by the same elements as in the previous step, but with roughness being present on the other side.
3. The sound power radiated in both cases is added up, resulting in the noise emitted by the wheelset and track as a consequence of the roughness on both sides.

When considering a bogie instead of a single wheelset, two wheelsets are taken into account. In this case, the previous three points are independently applied to both wheelsets. The incoherence of the combined roughness, particularly that of the wheel surfaces, allows the radiated power from the elements to be added. In this work, the same approach is applied to the Manchester Benchmark vehicle [25], which consists of four wheelsets.

5. Results

5.1. Inputs

Regarding the different dynamic simulations performed in this work, the following properties are considered:

- A track consisting of rails with UIC60 rail profile, with a gauge of 1435 mm, a rail inclination of 1:40, and a damping loss factor of 0.02 for the rails. The latter are supported by a spring–mass–spring system formed by the rail pad, sleeper, and ballast, the properties of which are converted to represent an equivalent continuously supported track assuming a sleeper span of 0.6 m. The rail pad has a stiffness of 715 MN/m in the vertical direction and 55 MN/m in the other two directions as well as a damping loss factor of 0.375. The sleeper has a mass of 244 kg, a length of 2500 mm in the lateral direction, a width of 250 mm in the longitudinal direction (running direction), and a height of 220 mm. The ballast has a stiffness of 70 MN/m in the vertical direction and 35 MN/m in the other two directions and a damping loss factor of 1.5.
- A wheelset with straight web wheels (see Fig. 2) and an approximate mass of 1050 kg. The wheels have a nominal diameter of 920 mm and a S1002 profile.
- A wheel/rail combined roughness spectrum according to the standard EN13979-1 [34] for cast iron brake blocks (see Fig. 5(a)), which is assumed to exist only in the normal direction to the contact plane, as indicated in Section 4.2. Also, the contact filter presented by Thompson [4], which corrects the effect of the roughness due to contact patch size (see Fig. 5(b)), is considered. In addition, a friction coefficient of 0.4 is taken into account for the wheel/rail interaction, which is representative of a dry contact condition [35].
- The Manchester Benchmark vehicle running on a curved track. As a result, one car body with two bogies, and thus four wheelsets in coasting condition, is analysed.

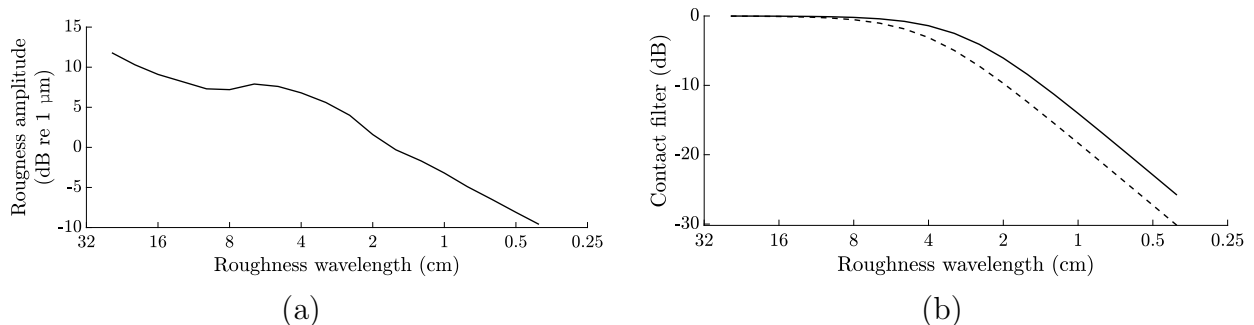


Fig. 5: (a) Roughness spectrum. (b) Contact filter for $a = 5$ mm (solid line) and $a = 7$ mm (dashed line).

5.2. Comparison of methodologies

The three-dimensional model presented in Section 2 is compared with the axisymmetric approach developed in Section 3. To do this, the Manchester Benchmark vehicle [25] is considered, running on a 300 m radius curve with 100 mm of superelevation and a speed of 75 km/h. The comparison concerns the frequency response function (FRF) in the radial-radial direction for the contact point of the outer wheel in the leading wheelset of the vehicle, as well as the sound power levels (SWL) of that wheelset due to the interaction of its wheels with the rails, evaluating it according to the method described in Section 4.2. As can be observed in the corresponding results depicted in Fig. 6, no significant differences are found between both approaches, whereas the computational performance of the axisymmetric model is two orders of magnitude higher (less than in the tangent case [15] due to the coupling of the different Fourier harmonics). Thus, the axisymmetric approach is preferred over the three-dimensional methodology.

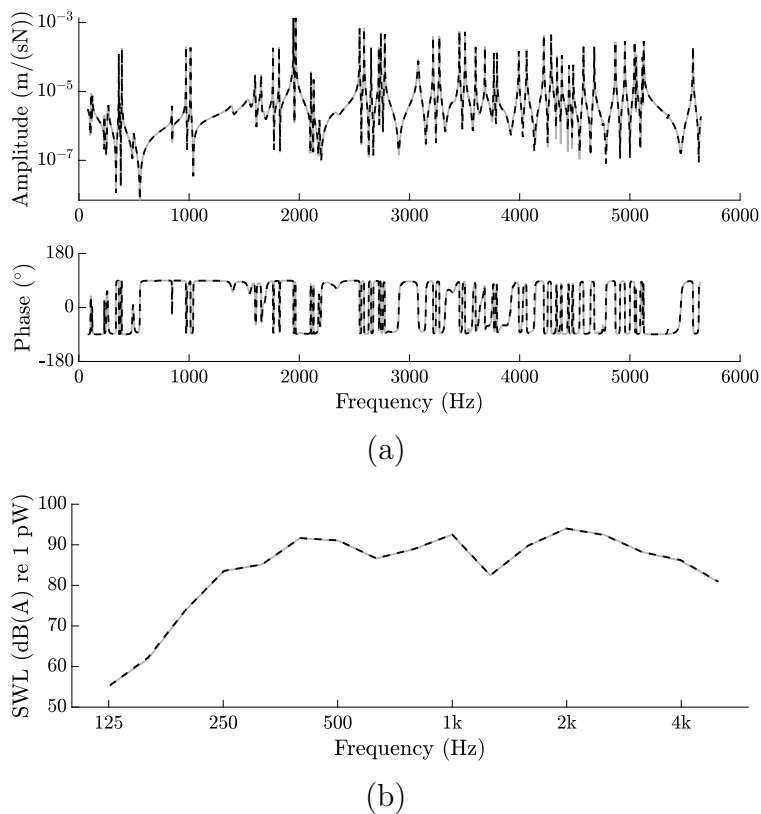


Fig. 6: Comparison of the three-dimensional (—) and axisymmetric (---) models for a vehicle speed of 75 km/h. (a) Radial-radial mobility at the contact point for the outer wheel of the leading wheelset. (b) Rolling noise radiated from this wheelset.

5.3. Rolling noise in curves

The noise radiation in two different curve situations is compared with a tangent track. The conditions considered are shown in Table 1, with h being the superelevation. Note that the latter is related to the cant angle γ as $h = \sin(\gamma)(g_T + b_R)$, where g_T is the track gauge and b_R the rail head width. The same vehicle speed is considered for all calculations in order

to reduce the influence of the roughness spectrum and contact filter, which have a variable frequency distribution depending on the speed.

Table 1: Running conditions.

	R_c (m)	V_v (m)	h (mm)
Curve 1	300	75	100
Curve 2	2000	75	30
Tangent	∞	75	0

The radiated noise due to the running of the Manchester Benchmark vehicle [25] through the three different tracks is depicted in Fig. 7. The frequency spectra of the three cases exhibit some noticeable differences, while smaller variations are found in the overall levels (see values in the figure legend). The overall level is determined by adding the sound power in each one-third octave frequency band after considering the contact filter proposed by Thompson [4] as well as the A-weighting filter [36], therefore expressed in dB(A) respect to 1 pW. Note that the levels in Fig. 7 correspond to the interaction of the four wheelsets of the vehicle with the rails, as explained in Section 4.2. Different radiation associated with each wheelset/track interaction is found, which will be explored later. Circulation on Curve 1 leads to higher overall noise from the wheels and rails, but lower radiation from the sleepers, causing a similar total overall noise when compared to a tangent track. On the other hand, for Curve 2 there is slightly less overall noise from all elements than in a straight section.

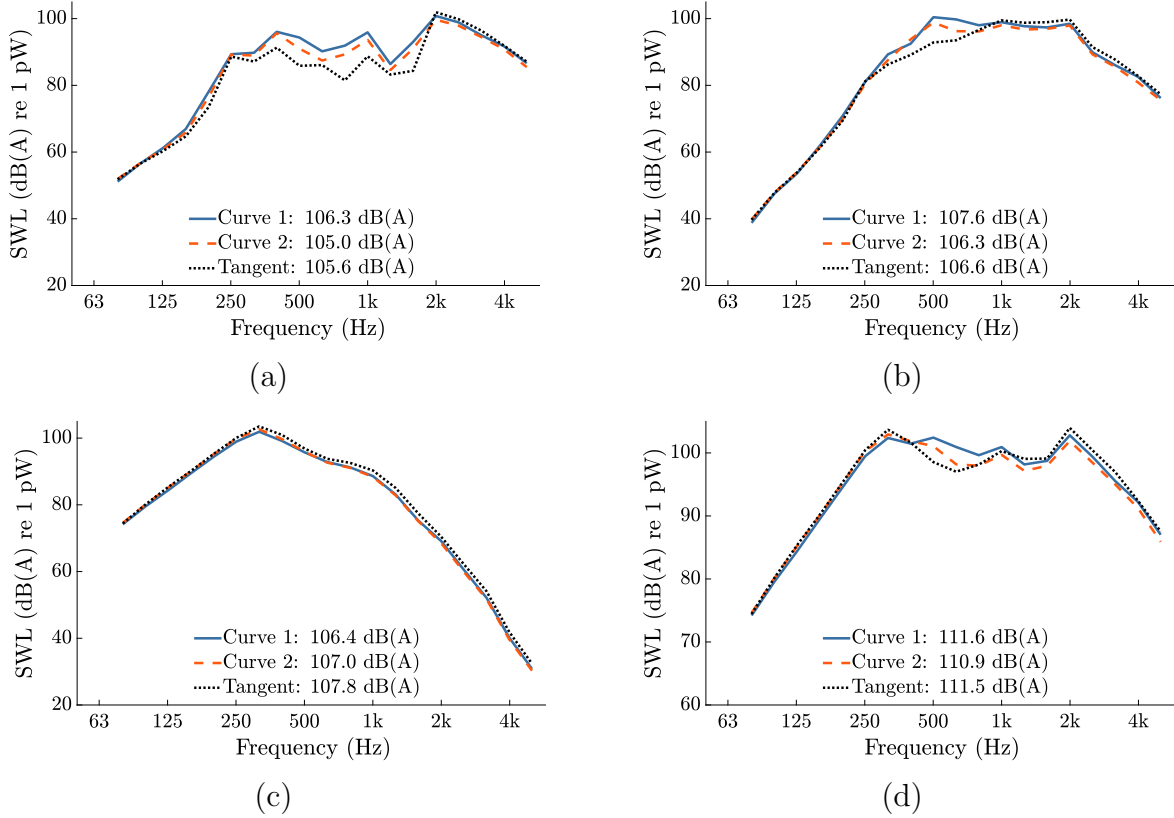
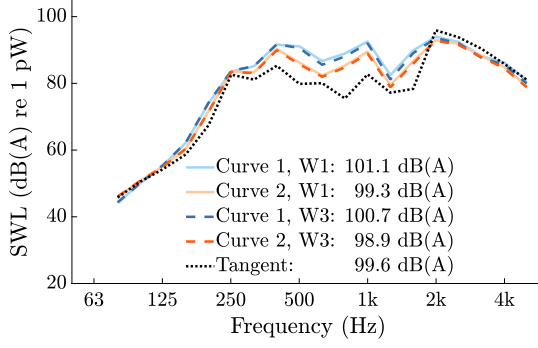
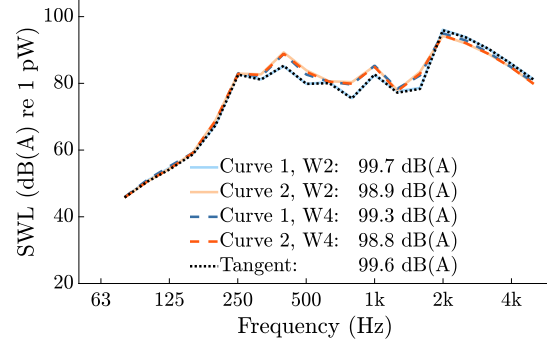


Fig. 7: SWL from the wheels (a), rails (b), and sleepers (c), as well as total noise (d) due to the running of the vehicle on the three tracks.

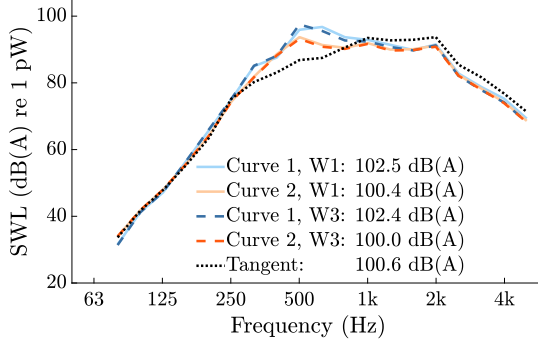
The interaction of each wheelset with the track results in a different noise radiation due to the variations in the associated steady-state condition. Fig. 8 shows the SWL corresponding to each wheelset/track interaction. The wheelsets are arranged in order from the front to the back, with the leading wheelset of the first bogie identified as W1 and the trailing wheelset of the second bogie as W4. In general terms, the noise associated with the interaction of the two leading wheelsets with the track is similar, as a result of having comparable positions in a curve, and the same can be said for the two trailing wheelsets.



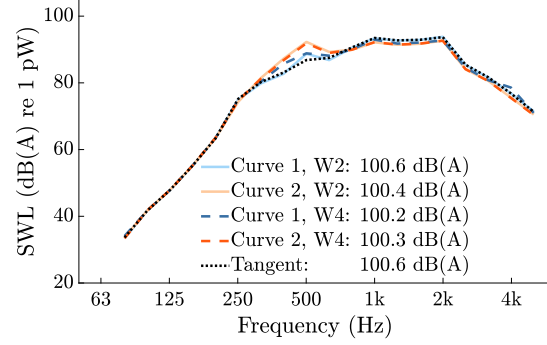
(a)



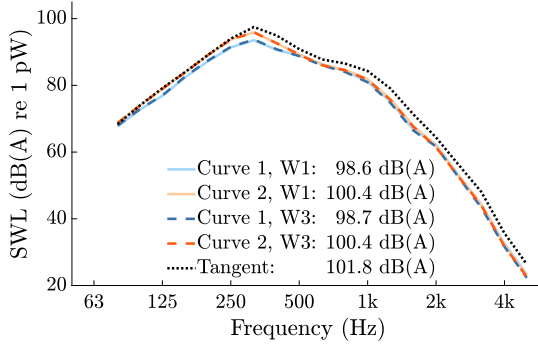
(b)



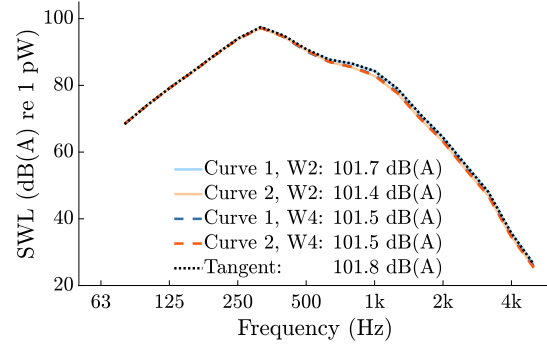
(c)



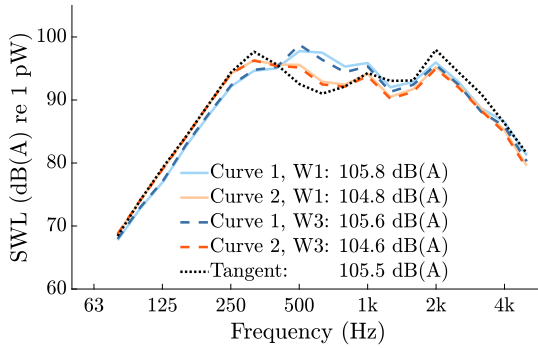
(d)



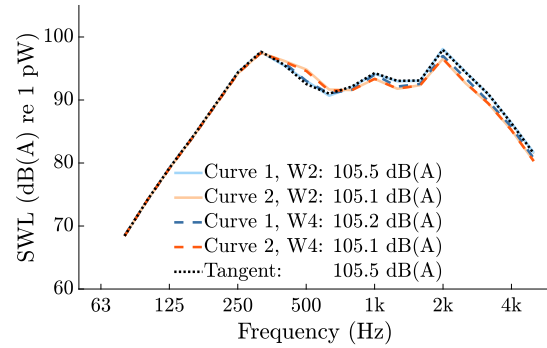
(e)



(f)



(g)



(h)

Fig. 8: SWL associated with the interaction of a single wheelset with the track. W_j refers to the j th wheelset. Left column: leading wheelsets. Right column: trailing wheelsets. First row: wheel. Second row: rail. Third row: sleeper. Fourth row: total.

The differences in the noise radiation associated with the three running conditions considered involve three main factors: changes in the interaction forces, an increase in the vertical-lateral coupling as the contact point moves away from the centre of the wheel tread and rail head, and the effect of the contact filter due to the size of the contact patch. As can be seen in Fig. 9, larger transverse displacements of the contact point across the wheel and rail profiles correspond to the left side (outer side as a right-hand curve is considered) of the leading wheelsets, especially for Curve 1 (higher curvature). Additionally, the legend in Fig. 9 displays the contact patch semi-length along the running direction a . In most cases, this variable is larger when running on a curve than on a tangent track, particularly for the outer side of the leading wheelsets (the ones that suffer higher lateral displacement of the contact position). As can be observed in Fig. 5(b), a larger contact patch semi-length a entails a higher impact of the contact filter, i.e. the SWL is more reduced in these cases.

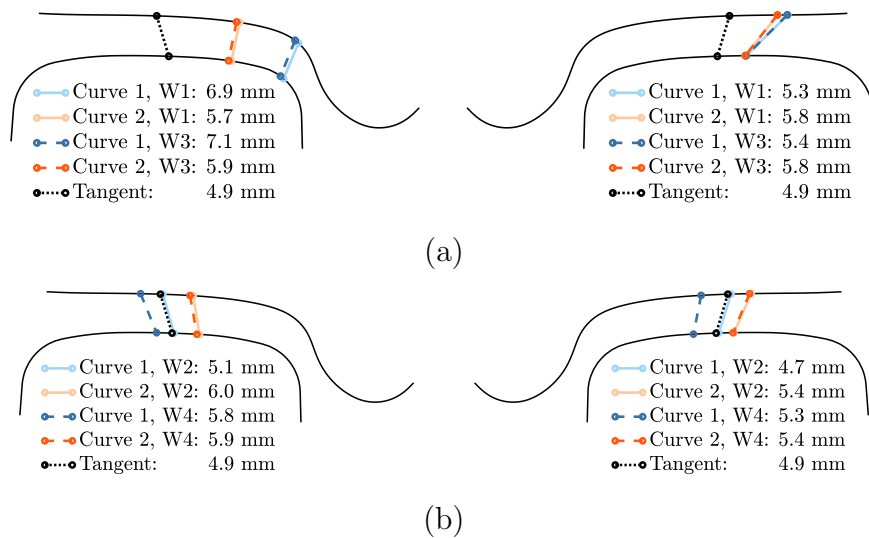


Fig. 9: Contact positions of the leading (a) and trailing (b) wheelsets in their interaction with the rails. The legends also display the contact patch semi-length along the running direction a . A right-hand curve is considered for the curving conditions.

In general, it is observed that the position of the wheel/rail contact is enough to explain the noise radiation in a curve, as the other steady-state contact variables are correlated with it. As the contact point moves away from the nominal position, although with some exceptions, it is found that: (1) the vertical force becomes lower, (2) the lateral force increases, (3) the vertical-lateral coupling is higher, and (4) the contact patch semi-length along the running direction a gets larger, increasing the impact of the contact filter. The first and last effects lead to lower noise radiation, and the opposite for the other two. Due to the opposite effect of them on the noise, different results are found for Curve 1 and Curve 2.

The wheel noise in the curving situations is higher than in the tangent track below about 2 kHz, where the lateral forces are found to be significantly higher in the curves. Although the vertical forces are lower in the curves, the vertical-lateral coupling plays an important role. Above 2 kHz, however, the difference in the lateral forces becomes smaller (still higher in the curves) and it is not enough to counter the effect of the contact filter. Thus, higher noise levels are found in this frequency range for the tangent track.

The SWL of the rail in a curve results from the contribution of both the lateral and vertical vibration. The former predominates in the low and medium frequency range (below approximately 1 kHz) and the latter at higher frequencies. Consequently, the noise radiated in the curving situations is higher than in the tangent track below 1 kHz (influenced by higher lateral force levels) and the opposite above 1 kHz. Here the vertical-lateral coupling and the contact filter effect are also important, although the two effects compensate with each other in the two curves.

The sleeper noise is governed by the vertical component of the interaction forces. The lateral radiation of the sleeper is negligible in comparison with the vertical one due to a small radiation area along with a lower vibration as a consequence of a lower rail pad stiffness in such direction, which produces a higher decoupling of this element from the rail. As a result, the sleeper noise is found to be lower in the curves than in the tangent track, especially for the wheelsets undergoing higher lateral displacements.

Due to different trends for the sleeper, rail, and wheel noise, the total sound power spectra in the curves and in the tangent track exhibit differences in their frequency content. In general, it can be seen that the leading wheelsets exhibit higher differences between the curves and tangent track, as a consequence of larger lateral displacements of the contact positions in the curves. Additionally, in the frequency range where the sleeper contribution to the total noise is predominant, that is, below about 400 Hz, the noise is found to be higher in tangent track. In the frequency range in which the rail noise is more important, i.e. between 400 Hz and 1 kHz, the sound radiation in the curves is higher. Above 1 kHz, where the wheel becomes predominant in the total radiation, the tangent SWL is higher again. It is worth noting that the previous trends correspond to a specific roughness spectrum and to the properties previously detailed for the wheelset and track.

6. Conclusions

In this study, a dynamic model of a flexible wheelset is proposed to evaluate the rolling noise radiation when operating on curved tracks. Two formulations are considered, both of them valid for any rotating structure with axial symmetry describing a generic trajectory (in particular, a curve of constant radius). On the one hand, a full three-dimensional numerical approach based on the FEM and, on the other, an axisymmetric model combining a FE approach for the wheelset cross-section and an analytical expansion of the response around the circumferential direction. In both cases, an Eulerian formulation is adopted to consider the inertial effects associated with the rotation and curved trajectory. It is shown that the results of both approaches present an excellent agreement, the axisymmetric one exhibiting significantly better computational performance.

The rolling noise radiation in two curve situations is analysed and compared with the case of the vehicle running on tangent track, the radius of the curves being 300 m and 2 km. The curve is found to influence the acoustic radiation for both cases. For the curve with a radius of 300 m, the overall wheel and rail noise is higher than in the tangent track, while the sleeper contribution is lower. For the curve with radius 2 km, instead, the overall levels of all three elements are smaller in the curve. Changes in the interaction forces, vertical-lateral coupling of the wheel and rail, and contact filter effect play an important role in rolling noise in curves. It is noted that the position of the wheel/rail contact point is strongly related to

the noise emitted by the wheelset and track in a curve. Thus, differences among the wheelsets in the vehicle are observed in terms of rolling noise radiation. Finally, the differences found in the overall total noise (sum of wheel, rail, and sleeper contributions) for both curving conditions compared with the tangent track are likely to depend on the roughness spectrum considered for the wheel and rail surfaces as well as on the properties of the wheelset and track. A more comprehensive study of noise emission in curves, in the form of a Design of Experiments considering the effect of different relevant parameters, such as the presence of traction or braking, is envisaged as a future development of this work.

Acknowledgements

This paper is part of the project PID2020-112886RA-I00, project PID2023-148483OB-I00, grant FPU18/03999, and grant EST22/00353 funded by MCIN/AEI/10.13039/501100011033 as well as by “ESF Investing in your future”. The authors also acknowledge Programa PROMETEO/2021/046 of Generalitat Valenciana.

Appendix A. Matrices and matrix operators

From Eq. (10), the matrix \mathbf{J} is given by:

$$\mathbf{J} = \begin{bmatrix} 0 & -1 & 0 \\ 1 & 0 & 0 \\ 0 & 0 & 0 \end{bmatrix}. \quad (\text{A.1})$$

The matrices \mathbf{J}_i in Eqs. (15), (21), (23), and (B.2–B.6) are sparse and thus they are defined in this appendix through their non-zero elements as follows:

$$\begin{aligned} \mathbf{J}_1 \text{ \{size } 3 \times (3 + 6m)\} : \\ (1, 7) = 1, \quad (1, 8) = 1, \quad (2, 2) = 2, \quad (3, 4) = -1, \quad (3, 5) = 1, \end{aligned} \quad (\text{A.2})$$

$$\begin{aligned} \mathbf{J}_2 \text{ \{size } 3 \times 1\} : \\ (2, 1) = 2z, \end{aligned} \quad (\text{A.3})$$

$$\begin{aligned} \mathbf{J}_3 = \sum_{i=1}^3 \sum_{j=i}^3 \omega_{ij}^2 \frac{\partial \mathbf{J}_3}{\partial \omega_{ij}^2} \text{ \{size } (3 + 6m) \times 1\} : \\ \frac{\partial \mathbf{J}_3}{\partial \omega_{11}^2} : (1, 1) = r, \quad (10, 1) = -\frac{r}{2}, \quad (11, 1) = \frac{r}{2}, \\ \frac{\partial \mathbf{J}_3}{\partial \omega_{22}^2} : (2, 1) = 2z, \\ \frac{\partial \mathbf{J}_3}{\partial \omega_{33}^2} : (1, 1) = r, \quad (10, 1) = \frac{r}{2}, \quad (11, 1) = -\frac{r}{2}, \\ \frac{\partial \mathbf{J}_3}{\partial \omega_{12}^2} : (7, 1) = z, \quad (8, 1) = z, \quad (9, 1) = r, \\ \frac{\partial \mathbf{J}_3}{\partial \omega_{23}^2} : (4, 1) = -z, \quad (5, 1) = z, \quad (6, 1) = -r, \\ \frac{\partial \mathbf{J}_3}{\partial \omega_{13}^2} : (13, 1) = -r, \quad (14, 1) = -r, \end{aligned} \quad (\text{A.4})$$

$$\begin{aligned}
\mathbf{J}_4 &= \sum_{i=1}^3 \sum_{j=i}^3 \omega_{ij}^2 \frac{\partial \mathbf{J}_4}{\partial \omega_{ij}^2} \{ \text{size } (3+6m) \times (3+6m) \} : \\
\frac{\partial \mathbf{J}_4}{\partial \omega_{11}^2} &: (1,) = 1, (3,) = 1, (4,) = \frac{1}{4}, (5,) = \frac{1}{4}, (7,) = \frac{3}{4}, (8,) = \frac{3}{4}, \\
&(1, 10) = -1, (1, 11) = 1, (3, 13) = 1, (3, 14) = 1, (4, 5) = \frac{1}{2}, (7, 8) = \frac{1}{2}, \\
&\left[\left[(6n-3+k,) = \frac{1}{2} \right]_{k=1,2,4,5} \right]_{n=2}^m, \left[\left[\left[(6n-j, 6n+9+k) = \frac{(-1)^k}{2}, \right. \right. \right. \\
&\left. \left. \left. (6n+j, 6n+12+k) = \frac{(-1)^j}{2} \right]_{j=1,2} \right]_{k=1,2} \right]_{n=1}^{m-2} \\
\frac{\partial \mathbf{J}_4}{\partial \omega_{22}^2} &: (2,) = 2, \left[(6n,) = 1, (6n+3,) = 1 \right]_{n=1}^m, \\
\frac{\partial \mathbf{J}_4}{\partial \omega_{33}^2} &: (1,) = 1, (3,) = 1, (4,) = \frac{3}{4}, (5,) = \frac{3}{4}, (7,) = \frac{1}{4}, (8,) = \frac{1}{4}, (1, 10) = 1, \\
&(1, 11) = -1, (3, 13) = -1, (3, 14) = -1, (4, 5) = -\frac{1}{2}, (7, 8) = -\frac{1}{2}, \\
&\left[\left[(6n-3+k,) = \frac{1}{2} \right]_{k=1,2,4,5} \right]_{n=2}^m, \left[\left[\left[(6n-j, 6n+9+k) = -\frac{(-1)^k}{2}, \right. \right. \right. \\
&\left. \left. \left. (6n+j, 6n+12+k) = -\frac{(-1)^j}{2} \right]_{j=1,2} \right]_{k=1,2} \right]_{n=1}^{m-2}, \\
\frac{\partial \mathbf{J}_4}{\partial \omega_{12}^2} &: (1, 9) = 2, (2, 7) = 2, (2, 8) = 2, (3, 6) = 2, \left[(6n-2, 6n+9) = 1, \right. \\
&(6n-1, 6n+9) = 1, (6n, 6n+7) = 1, (6n, 6n+8) = 1, \\
&(6n+1, 6n+6) = -1, (6n+2, 6n+6) = 1, (6n+3, 6n+4) = -1, \\
&\left. (6n+3, 6n+5) = 1 \right]_{n=1}^{m-1}, \\
\frac{\partial \mathbf{J}_4}{\partial \omega_{23}^2} &: (1, 6) = -2, (2, 4) = -2, (2, 5) = 2, (3, 9) = 2, \\
&\left[(6n-2, 6n+6) = -1, (6n-1, 6n+6) = -1, (6n, 6n+4) = -1, \right. \\
&(6n, 6n+5) = 1, (6n+1, 6n+9) = 1, (6n+2, 6n+9) = 1, \\
&\left. (6n+3, 6n+7) = -1, (6n+3, 6n+8) = -1 \right]_{n=1}^{m-1}, \\
\frac{\partial \mathbf{J}_4}{\partial \omega_{13}^2} &: (1, 13) = -2, (1, 14) = -2, (3, 10) = -2, (3, 11) = 2, (4, 7) = -1, \\
&(4, 8) = -1, (5, 7) = 1, (5, 8) = 1, \left[(6n-2, 6n+13) = -1, \right. \\
&(6n-2, 6n+14) = -1, (6n-1, 6n+13) = -1, (6n-1, 6n+14) = -1, \\
&(6n+1, 6n+10) = 1, (6n+1, 6n+11) = -1, (6n+2, 6n+10) = -1, \\
&\left. (6n+2, 6n+11) = 1 \right]_{n=1}^{m-2},
\end{aligned} \tag{A.5}$$

$$\begin{aligned}
\mathbf{J}_5 &= \sum_{i=1} \omega_i \frac{\partial \mathbf{J}_5}{\partial \omega_i} \{\text{size } (3+6m) \times 1\} : \\
\frac{\partial \mathbf{J}_5}{\partial \omega_1} &: (4, 1) = -z, \quad (5, 1) = z, \quad (6, 1) = r, \\
\frac{\partial \mathbf{J}_5}{\partial \omega_2} &: (3, 1) = -2r, \\
\frac{\partial \mathbf{J}_5}{\partial \omega_3} &: (7, 1) = -z, \quad (8, 1) = -z, \quad (9, 1) = r,
\end{aligned} \tag{A.6}$$

$$\begin{aligned}
\mathbf{J}_6 &= \sum_{i=1} \omega_i \frac{\partial \mathbf{J}_6}{\partial \omega_i} \{\text{size } (3+6m) \times 1\} : \\
\frac{\partial \mathbf{J}_6}{\partial \omega_1} &: (9, 1) = -2r, \\
\frac{\partial \mathbf{J}_6}{\partial \omega_2} &: (1, 1) = 4r, \\
\frac{\partial \mathbf{J}_6}{\partial \omega_3} &: (6, 1) = 2r,
\end{aligned} \tag{A.7}$$

$$\begin{aligned}
\mathbf{J}_7 &= \sum_{i=1} \omega_i \frac{\partial \mathbf{J}_7}{\partial \omega_i} \{\text{size } (3+6m) \times (3+6m)\} (\text{antisymmetric}) : \\
\frac{\partial \mathbf{J}_7}{\partial \omega_1} &: (1, 6) = 1, \quad (2, 4) = -1, \quad (2, 5) = 1, \quad (3, 9) = -1, \quad \left[(6n-2, 6n+6) = \frac{1}{2}, \right. \\
&\quad (6n-1, 6n+6) = \frac{1}{2}, \quad (6n, 6n+4) = -\frac{1}{2}, \quad (6n, 6n+5) = \frac{1}{2}, \\
&\quad (6n+1, 6n+9) = \frac{1}{2}, \quad (6n+2, 6n+9) = -\frac{1}{2}, \quad (6n+3, 6n+7) = -\frac{1}{2}, \\
&\quad \left. (6n+3, 6n+8) = -\frac{1}{2} \right]_{n=1}^{m-1}, \\
\frac{\partial \mathbf{J}_7}{\partial \omega_2} &: (1, 3) = -2, \quad (4, 8) = -1, \quad (5, 7) = 1, \\
&\quad \left[(6n-2, 6n+2) = -1, \quad (6n-1, 6n+1) = 1 \right]_{n=2}^m, \\
\frac{\partial \mathbf{J}_7}{\partial \omega_3} &: (1, 9) = 1, \quad (2, 7) = -1, \quad (2, 8) = -1, \quad (3, 6) = 1, \quad \left[(6n-2, 6n+9) = \frac{1}{2}, \right. \\
&\quad (6n-1, 6n+9) = \frac{1}{2}, \quad (6n, 6n+7) = -\frac{1}{2}, \quad (6n, 6n+8) = -\frac{1}{2}, \\
&\quad (6n+1, 6n+6) = -\frac{1}{2}, \quad (6n+2, 6n+6) = \frac{1}{2}, \quad (6n+3, 6n+4) = \frac{1}{2}, \\
&\quad \left. (6n+3, 6n+5) = -\frac{1}{2} \right]_{n=1}^{m-1},
\end{aligned} \tag{A.8}$$

$$\mathbf{J}_8 = \sum_{i=1} \omega_i \frac{\partial \mathbf{J}_8}{\partial \omega_i} \{\text{size } (3 + 6m) \times (3 + 6m)\} :$$

$$\begin{aligned} \frac{\partial \mathbf{J}_8}{\partial \omega_1} : (1, 9) = -2, (3, 6) = -2, \left[(6n - 2, 6n + 9) = -(n + 1), \right. \\ (6n - 1, 6n + 9) = -(n + 1), (6n, 6n + 7) = n, (6n, 6n + 8) = n, \\ (6n + 1, 6n + 6) = n + 1, (6n + 2, 6n + 6) = -(n + 1), \\ \left. (6n + 3, 6n + 4) = -n, (6n + 3, 6n + 5) = n \right]_{n=1}^{m-1}, \end{aligned}$$

$$\frac{\partial \mathbf{J}_8}{\partial \omega_2} : (1,) = 2, (3,) = 2, (4, 5) = 2, (7, 8) = -2, \tag{A.9}$$

$$\begin{aligned} \left[\left[(6n - 3 + k,) = 1 \right]_{k=1,2,4,5} \right]_{n=1}^m, \left[(6n - 2, 6n - 1) = 2n, \right. \\ \left. (6n + 1, 6n + 2) = -2n, \right]_{n=2}^m, \end{aligned}$$

$$\begin{aligned} \frac{\partial \mathbf{J}_8}{\partial \omega_3} : (1, 6) = 2, (3, 9) = -2, \left[(6n - 2, 6n + 6) = n + 1, \right. \\ (6n - 1, 6n + 6) = n + 1, (6n, 6n + 4) = -n, (6n, 6n + 5) = n, \\ (6n + 1, 6n + 9) = n + 1, (6n + 2, 6n + 9) = -(n + 1), \\ \left. (6n + 3, 6n + 7) = -n, (6n + 3, 6n + 8) = -n \right]_{n=1}^{m-1}, \end{aligned}$$

$$\mathbf{J}_9 \{\text{size } (3 + 6m) \times (3 + 6m)\} :$$

$$\left[(k,) = 2 \right]_{k=1,2,3}, \left[\left[(6n - 3 + k,) = 1 \right]_{k=1}^6 \right]_{n=1}^m, \tag{A.10}$$

$$\mathbf{J}_{10} \{\text{size } (3 + 6m) \times 1\} :$$

$$(3, 1) = -2r, \tag{A.11}$$

$$\mathbf{J}_{11} \{\text{size } (3 + 6m) \times (3 + 6m)\} (\text{antisymmetric}) :$$

$$(1, 3) = -2, \left[(6n - 2, 6n + 2) = -1, (6n - 2, 6n + 1) = n, \right. \tag{A.12}$$

$$\left. (6n - 1, 6n + 1) = 1, (6n - 1, 6n + 2) = -n, (6n, 6n + 3) = n \right]_{n=1}^m,$$

$$\mathbf{J}_{12} \{\text{size } (3 + 6m) \times 1\} :$$

$$(1, 1) = 2r, \tag{A.13}$$

$$\mathbf{J}_{13} \{\text{size } (3 + 6m) \times (3 + 6m)\} :$$

$$(1,) = 1, (3,) = 1, \left[\left[(6n - 3 + k,) = \frac{n^2 + 1}{2} \right]_{k=1,2,4,5}, \right.$$

$$\left[(6n - 3 + k,) = \frac{n^2}{2} \right]_{k=3,6}, (6n - 2, 6n - 1) = 2n, \tag{A.14}$$

$$(6n + 1, 6n + 2) = -2n \Big]_{n=1}^m,$$

where, as indicated in Section 3, m indicates the truncation harmonic on the expansion of the response along the circumferential direction. Regarding the notation in the previous equations, it is worth indicating the following aspects:

- An element (k, k) in the diagonal of a matrix is denoted as $(k,)$.
- Matrices \mathbf{J}_7 and \mathbf{J}_{11} are antisymmetric and therefore only the terms over the diagonal are given.
- The notation $\left[f(n) \right]_{n=j}^m$ indicates that f is evaluated for every integer n from j to m .
- The notation $\left[f(k) \right]_{k=r,s}$ indicates that f is evaluated for $k = r$ and $k = s$.
- The nested notation $\left[\left[f(k, n) \right]_{k=r,s} \right]_{n=j}^m$ indicates that f is evaluated for any combination of k and n .

Regarding the matrix $\tilde{\mathbf{D}}$ from Eq. (23), it is a square matrix of order $(6 + 12m)$, evaluated as follows:

$$\tilde{\mathbf{D}} = \begin{bmatrix} 2\mathbf{D} & \mathbf{0} & \cdots & \mathbf{0} \\ \mathbf{0} & \mathbf{D} & \cdots & \mathbf{0} \\ \vdots & \vdots & \ddots & \vdots \\ \mathbf{0} & \mathbf{0} & \cdots & \mathbf{D} \end{bmatrix}, \quad (\text{A.15})$$

where $\mathbf{0}$ is a square null matrix of order 6 and \mathbf{D} is the material stiffness matrix obtained from Hooke's Law, given by [23]:

$$\mathbf{D} = \frac{E}{(1 + \nu)(1 - 2\nu)} \begin{bmatrix} 1 - \nu & \nu & \nu & 0 & 0 & 0 \\ \nu & 1 - \nu & \nu & 0 & 0 & 0 \\ \nu & \nu & 1 - \nu & 0 & 0 & 0 \\ 0 & 0 & 0 & \frac{1-2\nu}{2} & 0 & 0 \\ 0 & 0 & 0 & 0 & \frac{1-2\nu}{2} & 0 \\ 0 & 0 & 0 & 0 & 0 & \frac{1-2\nu}{2} \end{bmatrix}, \quad (\text{A.16})$$

with E being the Young's modulus and ν the Poisson's ratio. In relation to the matrix operator $\tilde{\mathbf{L}}$, which allows the calculation of $\tilde{\mathbf{B}}$ in Eq. (23), it is a non-square matrix of dimensions $(6 + 12m) \times (3 + 6m)$, given by:

$$\tilde{\mathbf{L}} = \begin{bmatrix} \mathbf{L}_0 & \mathbf{0}_2 & \cdots & \mathbf{0}_2 \\ \mathbf{0}_1 & \mathbf{L}_1 & \cdots & \mathbf{0}_3 \\ \vdots & \vdots & \ddots & \vdots \\ \mathbf{0}_1 & \mathbf{0}_3 & \cdots & \mathbf{L}_n \end{bmatrix}, \quad (\text{A.17})$$

where $\mathbf{0}_1$, $\mathbf{0}_2$, and $\mathbf{0}_3$ are null matrices of dimensions 12×3 , 6×6 , and 12×6 , respectively, and the operators \mathbf{L}_0 and \mathbf{L}_n (with $n > 0$) are defined as follows:

$$\mathbf{L}_0 = \begin{bmatrix} \frac{\partial}{\partial r} & 0 & 0 \\ \frac{1}{r} & 0 & 0 \\ 0 & \frac{\partial}{\partial z} & 0 \\ \frac{\partial}{\partial z} & \frac{\partial}{\partial r} & 0 \\ 0 & 0 & \frac{\partial}{\partial r} - \frac{1}{r} \\ 0 & 0 & \frac{\partial}{\partial z} \end{bmatrix}. \quad (\text{A.18})$$

$$\mathbf{L}_n = \begin{bmatrix} \frac{\partial}{\partial r} & 0 & 0 & 0 & 0 & 0 \\ \frac{1}{r} & \frac{n}{r} & 0 & 0 & 0 & 0 \\ 0 & 0 & \frac{\partial}{\partial z} & 0 & 0 & 0 \\ \frac{\partial}{\partial z} & 0 & \frac{\partial}{\partial r} & 0 & 0 & 0 \\ -\frac{n}{r} & \frac{\partial}{\partial r} - \frac{1}{r} & 0 & 0 & 0 & 0 \\ 0 & \frac{\partial}{\partial z} & -\frac{n}{r} & 0 & 0 & 0 \\ 0 & 0 & 0 & \frac{\partial}{\partial r} & 0 & 0 \\ 0 & 0 & 0 & \frac{1}{r} & -\frac{n}{r} & 0 \\ 0 & 0 & 0 & 0 & 0 & \frac{\partial}{\partial z} \\ 0 & 0 & 0 & \frac{\partial}{\partial z} & 0 & \frac{\partial}{\partial r} \\ 0 & 0 & 0 & \frac{n}{r} & \frac{\partial}{\partial r} - \frac{1}{r} & 0 \\ 0 & 0 & 0 & 0 & \frac{\partial}{\partial z} & \frac{n}{r} \end{bmatrix}, \quad n = 1, \dots, m. \quad (\text{A.19})$$

Appendix B. Kinetic energy integration

In this appendix, a detailed term-by-term analytical integration of the kinetic energy in Eq. (7) around the circumferential direction is provided.

$$K_1 = \frac{1}{2} \dot{\mathbf{p}}_c^T \dot{\mathbf{p}}_c M, \quad (\text{B.1})$$

$$K_2 = \dot{\mathbf{p}}_c^T \tilde{\omega}_c \int_V \rho \Theta (\mathbf{u} + \mathbf{w}) dV = \pi \dot{\mathbf{p}}_c^T \tilde{\omega}_c \int_A \rho (\mathbf{J}_1 \mathbf{w}_h + \mathbf{J}_2) r dA, \quad (\text{B.2})$$

$$K_3 = \dot{\mathbf{p}}_c^T \int_V \rho \Theta \frac{D(\mathbf{u} + \mathbf{w})}{Dt} dV = \pi \dot{\mathbf{p}}_c^T \int_A \rho \mathbf{J}_1 \dot{\mathbf{w}}_h r dA, \quad (\text{B.3})$$

$$\begin{aligned} K_4 &= \frac{1}{2} \int_V \rho (\mathbf{u} + \mathbf{w})^T \Theta^T \tilde{\omega}_c^T \tilde{\omega}_c \Theta (\mathbf{u} + \mathbf{w}) dV \\ &= \frac{\pi}{2} \int_A \rho ((\omega_{11}^2 + \omega_{33}^2) r^2 + 2\omega_{22}^2 z^2) r dA + \pi \int_A \rho \mathbf{J}_3^T \mathbf{w}_h r dA \\ &\quad + \frac{\pi}{2} \int_A \rho \mathbf{w}_h^T \mathbf{J}_4 \mathbf{w}_h r dA, \end{aligned} \quad (\text{B.4})$$

$$\begin{aligned}
K_5 &= \frac{1}{2} \int_V \rho (\mathbf{u} + \mathbf{w})^T \Theta^T \tilde{\omega}_c^T \tilde{\omega}_c \Theta \frac{D(\mathbf{u} + \mathbf{w})}{Dt} dV = \Omega 2\pi\omega_2 \int_A \rho r^3 dA \\
&+ \pi \int_A \rho (\mathbf{J}_5^T + \mathbf{w}_h^T \mathbf{J}_7) \dot{\mathbf{w}}_h r dA + \Omega\pi \int_A \rho (\mathbf{J}_6^T + \mathbf{w}_h^T \mathbf{J}_8) \mathbf{w}_h r dA,
\end{aligned} \tag{B.5}$$

$$\begin{aligned}
K_t &= \frac{1}{2} \int_V \rho \frac{D(\mathbf{u} + \mathbf{w})^T}{Dt} \frac{D(\mathbf{u} + \mathbf{w})}{Dt} dV = \Omega^2 \pi \omega_2 \int_A \rho r^3 dA + \frac{\pi}{2} \int_A \rho \dot{\mathbf{w}}_h^T \mathbf{J}_9 \dot{\mathbf{w}}_h r dA \\
&+ \Omega\pi \int_A \rho (\mathbf{J}_{10}^T + \mathbf{w}_h^T \mathbf{J}_{11}) \dot{\mathbf{w}}_h r dA + \Omega^2 \pi \int_A \rho (\mathbf{J}_{12}^T + \mathbf{w}_h^T \mathbf{J}_{13}) \mathbf{w}_h r dA,
\end{aligned} \tag{B.6}$$

where $dV = rd\theta dA$ and the matrices \mathbf{J}_i are defined in the Appendix A.

References

- [1] D. J. Thompson, C. J. C. Jones, A review of the modelling of wheel/rail noise generation, *J. Sound Vib.* 231 (3) (2000) 519–536, <https://doi.org/10.1006/jsvi.1999.2542>.
- [2] M. J. Rudd, Wheel/rail noise—part II: Wheel squeal, *J. Sound Vib.* 46 (3) (1976) 381–394, [https://doi.org/10.1016/0022-460X\(76\)90862-2](https://doi.org/10.1016/0022-460X(76)90862-2).
- [3] I. Zenzerovic, W. Kropp, A. Pieringer, An engineering time-domain model for curve squeal: Tangential point-contact model and Green’s functions approach, *J. Sound Vib.* 376 (2016) 149–165, <https://doi.org/10.1016/j.jsv.2016.04.037>.
- [4] D. J. Thompson, *Railway Noise and Vibration. Mechanisms, Modelling and Means of Control*, Elsevier, 2009, ISBN: 978-0-08-045147-3, <https://doi.org/10.1016/B978-0-08-045147-3.X0023-0>.
- [5] S. L. Grassie, J. Kalousek, Rail corrugation: Characteristics, causes and treatments, *Proc. Inst. Mech. Eng., Part F: J. Rail Rapid Transit* 207 (1) (1993) 57–68, https://doi.org/10.1243/PIME_PROC_1993_207_227_02.
- [6] P. T. Torstensson, M. Schilke, Rail corrugation growth on small radius curves—measurements and validation of a numerical prediction model, *Wear* 303 (1) (2013) 381–396, <https://doi.org/10.1016/j.wear.2013.03.029>.
- [7] J. Wang, D. J. Thompson, G. Squicciarini, Rolling noise on curved track: an efficient time domain model including coupling between the two wheels and rails, in: *Noise and Vibration Mitigation for Rail Transportation Systems*, 2024, pp. 307–315, ISBN: 978-981-99-7852-6.
- [8] A. Wickens, *Fundamentals of Rail Vehicle Dynamics*, CRC Press, 2003, ISBN: 9780429224652, <https://doi.org/10.1201/9780203970997>.
- [9] K. Knothe, S. Stichel, *Rail Vehicle Dynamics*, Springer International Publishing, 2017, ISBN: 978-3-319-45376-7, <https://doi.org/10.1007/978-3-319-45376-7>.

- [10] S. Iwnicki, M. Spiryagin, C. Cole, T. McSweeney (Eds.), Handbook of Railway Vehicle Dynamics, Second Edition (2nd ed.), CRC Press, 2019, ISBN: 9780429469398, <https://doi.org/10.1201/9780429469398>.
- [11] S. Bruni, J. P. Meijaard, G. Rill, A. L. Schwab, State-of-the-art and challenges of railway and road vehicle dynamics with multibody dynamics approaches, *Multibody Syst. Dyn.* 49 (2020) 1–32, <https://doi.org/10.1007/s11044-020-09735-z>.
- [12] E. Di Gialleonardo, F. Braghin, S. Bruni, The influence of track modelling options on the simulation of rail vehicle dynamics, *J. Sound Vib.* 331 (19) (2012) 4246–4258, <https://doi.org/10.1016/j.jsv.2012.04.024>.
- [13] J. Martínez-Casas, L. Mazzola, L. Baeza, S. Bruni, Numerical estimation of stresses in railway axles using a train–track interaction model, *Int. J. Fatigue* 47 (2013) 18–30, <https://doi.org/10.1016/j.ijfatigue.2012.07.006>.
- [14] J. Martínez-Casas, E. Di Gialleonardo, S. Bruni, L. Baeza, A comprehensive model of the railway wheelset–track interaction in curves, *J. Sound Vib.* 333 (18) (2014) 4152–4169, <https://doi.org/10.1016/j.jsv.2014.03.032>.
- [15] V. T. Andrés, J. Martínez-Casas, F. D. Denia, D. J. Thompson, A model of a rotating railway wheel for the prediction of sound radiation, *J. Sound Vib.* 553 (2023) 117667, <https://doi.org/10.1016/j.jsv.2023.117667>.
- [16] VI-Grade GmbH, VI-Rail 2022.1 Documentation, VI-Grade Engineering Software & Services, 2022.
- [17] D. J. Thompson, Wheel-rail noise generation, part III: Rail vibration, *J. Sound Vib.* 161 (3) (1993) 421–446, doi: <https://doi.org/10.1006/jsvi.1993.1084>.
- [18] D. J. Mead, A general theory of harmonic wave propagation in linear periodic systems with multiple coupling, *J. Sound Vib.* 27 (2) (1973) 235–260, doi: [https://doi.org/10.1016/0022-460X\(73\)90064-3](https://doi.org/10.1016/0022-460X(73)90064-3).
- [19] D. J. Thompson, C. J. C. Jones, Sound radiation from a vibrating railway wheel, *J. Sound Vib.* 253 (2) (2002) 401–419, <https://doi.org/10.1006/jsvi.2001.4061>.
- [20] D. J. Thompson, M. H. A. Janssens, F. G. de Beer, Track Wheel Interaction Noise Software (TWINS) Theoretical Manual (version 3.4), TNO report, TNO Institute of Applied Physics, 2019.
- [21] G. K. Batchelor, An Introduction to Fluid Dynamics, Cambridge University Press, 2000, ISBN: 9780511800955, <https://doi.org/10.1017/CB09780511800955>.
- [22] R. B. Bird, W. E. Stewart, E. N. Lightfoot, Transport Phenomena, Revised 2nd Edition, John Wiley & Sons, 2006, ISBN: 978-0-470-11539-8.
- [23] O. C. Zienkiewicz, R. L. Taylor, J. Z. Zhu, The Finite Element Method: Its Basis and Fundamentals, 7th Edition, Butterworth-Heinemann, 2013, ISBN: 978-1-85617-633-0, <https://doi.org/10.1016/C2009-0-24909-9>.

- [24] M. Petyt, Introduction to Finite Element Vibration Analysis, 2nd Edition, Cambridge University Press, 2010, ISBN: 9780521191609, <https://doi.org/10.1017/CB09780511761195>.
- [25] S. Iwnicki, Manchester benchmarks for rail vehicle simulation, *Veh. Syst. Dyn.* 30 (3-4) (1998) 295–313, <https://doi.org/10.1080/00423119808969454>.
- [26] V. T. Andrés, J. Martínez-Casas, F. D. Denia, D. J. Thompson, Influence study of rail geometry and track properties on railway rolling noise, *J. Sound Vib.* 525 (2022) 116701, <https://doi.org/10.1016/j.jsv.2021.116701>.
- [27] W. Liu, L. Du, W. Liu, D. J. Thompson, Dynamic response of a curved railway track subjected to harmonic loads based on the periodic structure theory, *Proc. Inst. Mech. Eng., Part F: J. Rail Rapid Transit* 232 (7) (2018) 1932–1950, <https://doi.org/10.1177/0954409718754470>.
- [28] D. J. Thompson, Wheel-rail noise generation, part I: Introduction and interaction model, *J. Sound Vib.* 161 (3) (1993) 387–400, doi: <https://doi.org/10.1006/jsvi.1993.1082>.
- [29] A. Gross-Thebing, Frequency-dependent creep coefficients for three-dimensional rolling contact problems, *Veh. Syst. Dyn.* 18 (6) (1989) 359–374, doi: <https://doi.org/10.1080/00423118908968927>.
- [30] D. J. Thompson, Wheel-rail noise: theoretical modelling of the generation of vibrations, PhD Thesis, University of Southampton (1990).
- [31] D. J. Thompson, Wheel-rail noise generation, part IV: Contact zone and results, *J. Sound Vib.* 161 (3) (1993) 447–466, doi: <http://dx.doi.org/10.1006/jsvi.1993.1085>.
- [32] J. J. Kalker, Wheel-rail rolling contact theory, *Wear* 144 (1) (1991) 243–261, doi: [https://doi.org/10.1016/0043-1648\(91\)90018-P](https://doi.org/10.1016/0043-1648(91)90018-P).
- [33] J. J. Kalker, A fast algorithm for the simplified theory of rolling contact, *Veh. Syst. Dyn.* 11 (1) (1982) 1–13, doi: <https://doi.org/10.1080/00423118208968684>.
- [34] Railway applications – Wheelsets and bogies – Monobloc wheels – Technical approval procedure – Part 1: Forged and rolled wheels. EN 13979-1:2020, European Committee for Standardization (2020).
- [35] U. Olofsson, Chapter 17 - Adhesion and friction modification, in: R. Lewis, U. Olofsson (Eds.), *Wheel–Rail Interface Handbook*, Woodhead Publishing, 2009, pp. 510–527, ISBN: 978-1-84569-412-8, <https://doi.org/10.1533/9781845696788.1.510>.
- [36] Electroacoustics – Sound level meters – Part 1: Specifications. IEC 61672-1:2013, International Electrotechnical Commission (2013).